Zonal-based high-performance control in adaptive optics systems with application to astronomy and satellite tracking

Léonard Prengère, Caroline Kulcsár, Henri-François Raynaud

▶ **To cite this version:**

HAL Id: hal-03169469

https://hal-iogs.archives-ouvertes.fr/hal-03169469

Submitted on 29 Mar 2024

Zonal-based high-performance control in adaptive optics systems with application to astronomy and satellite tracking

LÈONARD PRENGÈRE,* CAROLINE KULCSÁR, [ID] AND HENRI-FRANÇOIS RAYNAUD

Université Paris-Saclay, Institut d'Optique Graduate School, CNRS, Laboratoire Charles Fabry, 91127, Palaiseau, France
Corresponding author: leonard.prengere@institutoptique.fr

This paper presents a model-based approach to adaptive optics (AO) control based on a zonal (i.e., pixelized) representation of the incoming atmospheric turbulence. Describing the turbulence on a zonal basis enables the encapsulation of the standard frozen-flow assumption into a control-oriented model. A multilayer zonal model is proposed for single-conjugate AO (SCAO) systems. It includes an edge compensation mechanism involving limited support, which results in a sparser model structure. To further reduce the computational complexity, new resultant zonal models localized in the telescope pupil are proposed, with AR1 or AR2 structures, that match the spatial and temporal cross-correlations of the incoming turbulence. The global performance of the resulting linear quadratic Gaussian (LQG) regulator is evaluated using end-to-end simulations and compared to several existing controllers for two different configurations: a very large telescope SCAO and low earth orbit satellite tracking. The results show the high potential of the new approach and highlight possible trade-offs between the performance and complexity.   © 2020

1. INTRODUCTION

Atmospheric turbulence introduces wavefront distortions that degrade the images acquired by ground-based telescopes [1]. Adaptive optics (AO) systems can compensate for these nefarious effects in real time, using deformable mirrors (DMs) inserted in the optical path. Wavefront sensors (WFSs) provide discrete-time wavefront measurements used by a digital controller to compute the DM commands in a control loop. There are delays between the WFS measurements and the application of corresponding DM commands, and the turbulent phase evolves during the lag, limiting the efficiency of the phase correction. This phase evolution leads to a temporal error commonly named servo-lag error, which is a major limitation in high-performance AO systems such as the exoplanet detection instruments Gemini Planet Imager (GPI) [2] or SPHERE [3].

The most commonly used AO controller is the standard integrator (or integral action regulator), which was already operational on the first AO system in 1989, with COME-ON [4,5]. As the integrator is known to suffer from servo-lag error, predictive controllers have been proposed before the 2000s [6,7] and tested on the sky as early as 1999 [8]. Optimal (minimum variance) linear quadratic Gaussian (LQG) regulators made a step further with an explicit prediction of the phase, thanks to a Kalman filter based on a dynamic stochastic phase model [9–12]. This phase prediction capability allows for servo-lag

error reduction through the compensation of vibrations, wind-shake, and atmospheric turbulence. Several on-sky experiments have been realized with full [13,14] or low-order [15–18] LQG regulators. Two operational systems are currently equipped with LQG regulators: SPHERE-SAXO for tip-tilt correction [17] and GPI for the correction of three low-order modes (tip, tilt, and focus) [18].

Boiling turbulence models in Zernike basis using auto-regressive (AR) models of order 1 (AR1) [9,19] have been proposed for their low complexity. Turbulence AR Zernike models of order 2 (AR2) have been used successfully on the sky with LQG control on the CANARY demonstrator [14]. Frozen flow behaviors of turbulence layers are frequent and can contribute significantly to the controllable phase, specifically for high spatial frequency modes, as explained in [20]. This motivates modeling of the frozen flow behavior to benefit from a better phase prediction at short time scales, as in [21]. The zonal basis also allows a natural description of translations using simple nonlocalized operators, whereas it is less convenient for a modal-based description localized in the telescope pupil. A convenient Fourier domain frozen flow model has therefore been proposed by [22] for a fast wavefront reconstruction. However, measurements are needed in the Fourier domain at each iteration, and obtained through an iterative transformation using discrete Fourier transform. A Frozen LQG combining Zernike and

zonal basis has been proposed [23] to account for the frozen flow hypothesis while keeping a boiling-type turbulence model. To do so, phase prediction is performed in zonal basis by translating the phase screen estimated thanks to a Kalman filter in Zernike basis.

The zonal basis allows for a very simple description of the frozen flow, and several approaches have been proposed to derive Markovian quasi-frozen flow models. A zonal multilayer atmosphere model has been used to design an LQG regulator for multiconjugate AO (MCAO) in [24] or for multi-object AO in [25]. Under the spatially invariant and frozen flow hypothesis, an LQG regulator with a distributed Kalman filter (LQG-DKF) has been proposed for MCAO in [26,27]. The method, as shown later in this paper, suffers in SCAO from performance degradation due to approximations in the measurement model and to the finiteness of the telescope pupil.

In this article we revisit the works of [24,25,28,29] to propose new zonal models that account for a frozen flow behavior of the turbulence. A multilayer zonal-based model with frozen flow assumption, similar to the hypothesis in [24,25], is proposed for SCAO systems but with an edge compensation mechanism that involves limited support, inducing a sparser model structure compared to the literature. To further reduce the computational complexity that can be problematic for multilayer atmosphere models of AO systems, we also propose, in line with the spatio-angular LQG (SA-LQG) [25,29], new resultant (i.e., defined in the telescope pupil) models with AR1 and AR2 structures in a zonal basis. The resultant AR1 model features a sparser transition matrix, and the AR2 models take full advantage of spatial and temporal cross-correlations. (Note: They are not supposed to have diagonal matrix parameters.) All these quasi-frozen flow models depend on atmosphere priors, which can be estimated from AO telemetry [20,30] or SCIDAR measurements [31–33].

Global control performance of the corresponding zonal-based LQG regulators is evaluated, thanks to end-to-end simulations with the object-oriented MATLAB adaptive optics (OOMAO) [34] simulator. The use of priors naturally raises the question of robustness in performance to errors in particular with respect to the wind profile, which we also address. The many LQG regulators (eight in total) are compared in two quite different configurations: an astronomical case of the very large telescope Nasmyth adaptive optics system (VLT-NAOS) type, and a satellite tracking case with a low earth orbit (LEO) configuration similar to [35]. Our results show the high potential of the new regulators, with impressive results in the satellite case, and highlight the possible trade-offs between the performance and complexity.

The paper has seven sections. Section 2 introduces the multilayer frozen flow state space modeling for LQG regulators. A first control performance study is conducted in Section 3 for LQG regulators based on different models of disturbance and WFS, including the spatially invariant LQG-DKF, allowing us to give orientations for model choices and parameters. To reduce computational complexity, Section 4 presents the derivation of the resultant AR models of order 1 and 2. In Section 5, end-to-end simulations in the VLT-NAOS-like case are performed for different turbulence behaviors. Multilayer and resultant zonal-based LQG regulators are compared against a standard integral

action controller, LQG regulators based on Zernike AR2 boiling models similar to the ones tested on sky [14], and against the frozen LQG [23] adapted to a multilayer atmosphere model. The performance robustness to errors on the wind profile is also evaluated. In Section 6, a performance assessment in the LEO satellite tracking case is conducted, together with an evaluation of performance robustness to the wind parameters of the ground layer and an assessment of the control performance when the signal-to-noise ratio (SNR) decreases. Finally, conclusions and perspectives are presented in Section 7.

2. ZONAL LQG REGULATOR UNDER FROZEN FLOW HYPOTHESIS

AO systems include real-time controllers that compute discrete time commands to be applied to the DM through a zero-order hold. It has been shown in [11] that the optimal continuous time optimal minimum variance control problem could be solved equivalently using a discrete time formulation. Each discrete time quantity then corresponds to the average of its continuous time value over one sampling period T, where T is the AO loop sampling period. This optimal control can be obtained under the form of an LQG controller if one can built a linear state-space representation of the AO loop including the disturbance. After a short reminder of the LQG AO control principle and equations (in Section 2.A), we focus in Sections 2.B and 2.C on the design of an adequate state-space model of the disturbance. Section 2.D details the measurement model associated with the disturbance state-space representation.

A. LQG Regulator for SCAO Systems

A block diagram presenting the principle of an AO loop is given in Fig. 1. The LQG regulator minimizes the residual phase variance ϕ^{res} [11]. At time $t = kT$, the optimal control u_k^{opt} is obtained by minimizing the criterion,

$$J_k^{\mathrm{d}}(u_k) \triangleq \mathrm{E}(||\phi_k^{\mathrm{res}}||^2|\mathfrak{J}_k) \triangleq \mathrm{trace}\left(\mathrm{Var}(\phi_k^{\mathrm{res}}|\mathfrak{J}_k)\right), \quad \textbf{(1)}$$

where $\phi^{\mathrm{res}} = \phi^{\mathrm{Tel}} - \phi^{\mathrm{cor}}$ is the residual phase in the telescope pupil and $\mathfrak{J}_k = \{y_0, \ldots, y_k, u_0, \ldots, u_{k-1}\}$ represents all past information (WFS measurements y and DM commands u). The turbulent phase in the volume restricted to the telescope pupil footprints is denoted by ϕ^{Tel}, and ϕ^{cor} is the correction phase generated by the DM. The DM is considered here to have a settling time fast enough with respect to the AO loop sampling period so that its dynamics can be neglected. However, a DM with slower response and/or badly damped dynamics could be considered as well to compensate for possible performance degradation, as explained in [10,36].

As $\phi_k^{\mathrm{cor}} = Nu_{k-1}$ and $\phi_k^{\mathrm{res}} = \phi_k^{\mathrm{Tel}} - \phi_k^{\mathrm{cor}}$ (see Fig. 1), the optimal control is written as

$$u_k^{\mathrm{opt}} \triangleq \arg\min_{u_k}\left(J_k^{\mathrm{d}}(u_k)\right) = (N^{\mathrm{T}}N)^{-1}N^{\mathrm{T}}\hat{\phi}_{k+1|k}^{\mathrm{Tel}}, \quad \textbf{(2)}$$

where $\hat{\phi}_{k+1|k}^{\mathrm{Tel}} = \mathrm{E}(\phi_{k+1}^{\mathrm{Tel}}|\mathfrak{J}_k)$ is the minimum variance estimate of $\phi_{k+1}^{\mathrm{Tel}}$ knowing $\mathfrak{J}_k$. The prediction $\hat{\phi}_{k+1|k}^{\mathrm{Tel}}$ can be computed by a Kalman filter, assuming that a Markovian state-space representation can be provided, for example, under the form
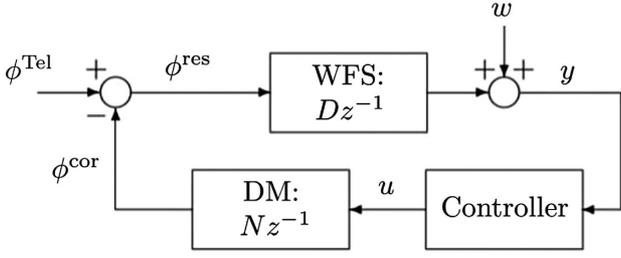
Fig. 1. Block diagram of an AO control loop. All blocks are linear and the total loop delay is supposed here to be two frames. The incoming (multilayer) turbulence above the telescope is denoted by ϕ^{Tel}.

$$X_{k+1} = AX_k + \Gamma v_k, \tag{3}$$

$$\phi_k^{\text{Tel}} = C_1 X_k, \tag{4}$$

$$y_k = CX_k + w_k - DN u_{k-2}, \tag{5}$$

where A, Γ and C_1 depend on the chosen disturbance model, C depends on the chosen measurement model, and $\{v\}$ and $\{w\}$ are mutually independent Gaussian white noises with known covariance matrices Σ_v and Σ_w, respectively. The matrix DN corresponds to the interaction matrix M_{int}, and appears in the measurement model in Eq. (5) because the WFS provides closed-loop measurements y (see Fig. 1). In this paper, the state vector X_k stores the turbulent phase temporal occurrences needed to describe the dynamical model. The predicted state $\hat{X}_{k+1|k}$ is recursively updated by the Kalman filter prediction equation,

$$\hat{X}_{k+1|k} = (A - L_\infty C)\hat{X}_{k|k-1} + L_\infty(y_k + M_{\text{int}} u_{k-2}), \tag{6}$$

where L_∞ is the asymptotic Kalman gain, computed offline from the solution of the discrete algebraic Riccati equation (see [37]),

$$L_\infty = A\Sigma_\infty C^{\text{T}}(C\Sigma_\infty C^{\text{T}} + \Sigma_w)^{-1}, \tag{7}$$

$$\begin{aligned}\Sigma_\infty = {} & A\Sigma_\infty A^{\text{T}} + \Gamma \Sigma_v \Gamma^{\text{T}} \\ & - A\Sigma_\infty C^{\text{T}}(C\Sigma_\infty C^{\text{T}} + \Sigma_w)^{-1}C\Sigma_\infty A^{\text{T}},\end{aligned} \tag{8}$$

where Σ_∞ is the asymptotic estimation error covariance matrix. The prediction $\hat{\phi}_{k+1|k}^{\text{Tel}}$ is obtained from $\hat{X}_{k+1|k}$ using Eq. (4), so

$$\hat{\phi}_{k+1|k}^{\text{Tel}} = C_1 \hat{X}_{k+1|k}. \tag{9}$$

The optimal control is readily obtained through Eqs. (9), (6), and (2) as soon as a state representation has been established. The purpose of the next two sections (2.B and 2.C) is to build a state-space representation in the form of Eqs. (3–5) under the hypothesis of a frozen flow atmospheric turbulence.

B. From Pure Frozen Flow to Localized Quasi-Frozen Flow Models

The frozen flow (or Taylor) hypothesis has been considered in several works for control-oriented atmospheric turbulence

modeling [23–27,38–41]. Each layer is moving according to a pure translation, and can therefore be expressed with a spatially invariant convolution equation,

$$\phi_{k+1} = h * \phi_k, \tag{10}$$

where h is the two-dimensional (2D) convolution kernel describing the translation, and ϕ_k is the infinite dimensional turbulent phase layer at time k. For a spatially sampled turbulence layer, ϕ can be represented by a 2D Gaussian stationary discrete random field with zero mean and spatial covariance C_ϕ. To design an optimal controller implementable in finite dimension, a finite-dimensional Markovian dynamical model of the atmospheric perturbation is needed, as explained in [38]. To update the portion ϕ^{Tel} of the turbulence located inside the telescope pupil $\mathcal{P}$, the convolution product from Eq. (10) uses points that are either inside $\mathcal{P}$, or in a finite area $\mathcal{E}$ outside the telescope pupil. The phase points in $\mathcal{E}$ shall be denoted by ϕ^{Edge} (see Fig. 2). The domain $\mathcal{E}$ contains points needed to compute ϕ_{k+1}^{Tel}, so its size depends on the wind direction and norm (for each layer) and on the AO loop frequency. The convolution product in Eq. (10) for the phase points inside $\mathcal{P}$ can also be expressed with matrix vector products as

$$\phi_{k+1}^{\text{Tel}} = A_{\text{Tel}}\phi_k^{\text{Tel}} + A_{\text{Edge}}\phi_k^{\text{Edge}}, \tag{11}$$

where A_{Tel} and A_{Edge} simply code the application of h to phase points in $\mathcal{P}$ and $\mathcal{E}$, respectively. This model is not localized, as ϕ_k^{Edge} cannot be computed recursively from past values of ϕ^{Tel} and ϕ^{Edge}. To localize it in the telescope pupil, so that the phase evolution can be represented on a finite support, additional information on ϕ_k^{Edge} is needed. The simplest solution is to assume that we have no clues about points outside the telescope pupil, so we take $\phi_k^{\text{Edge}} = 0$. This assumption leads to the Markovian dynamical model,

$$\phi_{k+1}^{\text{Tel}} = A\phi_k^{\text{Tel}} + v_k, \tag{12}$$

where $A = A_{\text{Tel}}$ and $\{v\}$ is a Gaussian and temporally white noise that ensures adequate spatial statistics for ϕ through

$$\Sigma_v = E(v_k v_k^{\text{T}}) = \Sigma_\phi - A\Sigma_\phi A^{\text{T}}, \tag{13}$$

where $\Sigma_\phi \triangleq E(\phi^{\text{Tel}}(\phi^{\text{Tel}})^{\text{T}}) \triangleq \text{Var}(\phi^{\text{Tel}})$ is the covariance matrix of the sampled turbulent phase and is evaluated from the spatial covariance function C_ϕ. Due to stationarity, C_ϕ only depends on the distance ρ between two phase points [1]. Under von Kármán statistics, it is given by

$$\begin{aligned}C_\phi(\rho) = {} & \left(\frac{L_0}{r_0}\right)^{5/3}\left[\left(\frac{24}{5}\right)\Gamma(6/5)\right]^{5/6}\frac{\Gamma(11/6)}{2^{5/6}\pi^{8/3}}\left(\frac{2\pi\rho}{L_0}\right)^{5/6} \\ & \times K_{5/6}\left(\frac{2\pi\rho}{L_0}\right),\end{aligned} \tag{14}$$

where Γ is Euler's Gamma function, $K_{5/6}$ is a modified Bessel function of the 2nd kind, with order 5/6, and the Fried parameter r_0 and the outer scale L_0 are two macroscopic turbulent parameters [1]. For $\rho = 0$, we recover the theoretical variance σ_ϕ^2 of one phase point, so
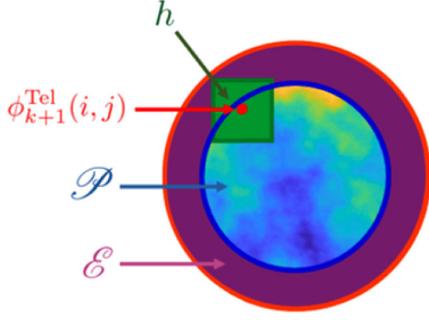
Fig. 2. Principle of the update step for the frozen flow dynamical model in Eq. (11). $\mathcal{P}$ is the telescope pupil and $\mathcal{E}$ is the set of points outside $\mathcal{P}$ that are needed for the update of Eq. (11). As an example, the point $\phi_{k+1}^{\text{Tel}}(i, j)$ located at coordinates (i, j) has been updated with the convolution kernel h from Eq. (10) using points $\phi_k^{\text{Edge}} \in \mathcal{E}$ and $\phi_k^{\text{Tel}} \in \mathcal{P}$.

Fig. 3. Patch $\mathcal{K}(i, j)$ containing the subset of points used to estimate the phase point with coordinates (i, j) in $\mathcal{E}$. The width of the intersection between $\mathcal{K}(i, j)$ and $\mathcal{P}$ is denoted by r. The point in $\mathcal{E}$ located at the furthest distance from $\mathcal{P}$ is denoted by f.

$$\sigma_\phi^2 = C_\phi(0) = \left(\frac{L_0}{r_0}\right)^{5/3}\left[\left(\frac{24}{5}\right)\Gamma(6/5)\right]^{5/6}\frac{\Gamma(11/6)}{2^{5/6}\pi^{8/3}}\frac{\Gamma(5/6)}{2^{1/6}}. \tag{15}$$

As A_{Tel} is nilpotent, the dynamical model in Eq. (12) is obviously stable. However, as pointed out by [23,29], this solution leads to poor performance and a maximum a posteriori (MAP) estimation of ϕ_k^{Edge}, knowing ϕ_k^{Tel} (i.e., a static minimum variance estimation) is known to give much better results [23–25,29,38].

C. Stochastic Dynamical Model with Edge Compensation

This MAP estimator requires only prior knowledge of the spatial covariance C_ϕ and can be written in compact form as

$$\hat{\phi}^{\text{Edge}} = \text{E}(\phi^{\text{Edge}}|\phi^{\text{Tel}}) = M_{\text{MAP}}\phi^{\text{Tel}}, \tag{16}$$

where M_{MAP} is the MAP reconstruction matrix,

$$M_{\text{MAP}} = \text{Cov}(\phi^{\text{Edge}}, \phi^{\text{Tel}})\Sigma_\phi^{-1}, \tag{17}$$

with $\text{Cov}(\phi^{\text{Edge}}, \phi^{\text{Tel}})$ the cross-covariance matrix of ϕ^{Edge} and ϕ^{Tel}. We then replace ϕ^{Edge} in Eq. (11) by $\hat{\phi}^{\text{Edge}}$ in Eq. (16) and define the dynamical stochastic model with edge compensation as

$$\phi_{k+1}^{\text{Tel}} = \left(A_{\text{Tel}} + A_{\text{Edge}}M_{\text{MAP}}\right)\phi_k^{\text{Tel}} + v_k, \tag{18}$$

where, as previously, the Gaussian white noise $\{v\}$ has a variance Σ_v chosen to ensure proper statistics:

$$\Sigma_v = \Sigma_\phi - \left(A_{\text{Tel}} + A_{\text{Edge}}M_{\text{MAP}}\right)\Sigma_\phi\left(A_{\text{Tel}} + A_{\text{Edge}}M_{\text{MAP}}\right)^{\text{T}}. \tag{19}$$

From Eq. (14), it is clear that the matrix M_{MAP} defined in Eq. (17) is independent from r_0 and thus, also from the layers, and only depends on the global outer scale L_0. As pointed out in previous works [42,43], to simulate very large turbulent and sampled phase screens, a static MAP estimation needs very few points insi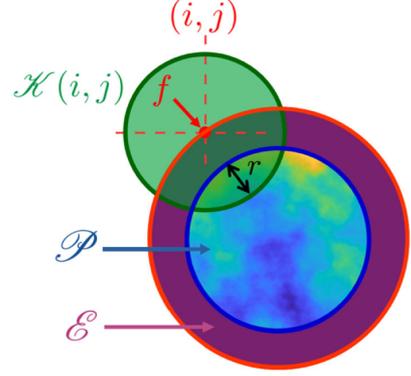de the telescope pupil to deliver spatial statistics that are consistent with theoretical values. We define the circular patch $\mathcal{K}(i, j)$ centered in (i, j) and containing the points of $\mathcal{P}$ used in Eq. (16) to estimate the point in $\mathcal{E}$ with coordinate (i, j). This circular patch $\mathcal{K}(i, j)$ has an intersection with $\mathcal{P}$ of width denoted by r, as illustrated in Fig. 3. The quality of the MAP reconstruction will thus depend on r.

To determine an appropriate value of r, we introduce the quality-of-reconstruction criterion,

$$Q_f(r) = 1 - \frac{\sigma_{\tilde{f}}^{2,l}(r)}{\sigma_\phi^{2,l}}, \tag{20}$$

which represents a normalized estimation error variance. In this formula, $\sigma_{\tilde{f}}^{2,l}(r)$ is the MAP estimator error variance of the furthest point f in $\mathcal{E}$ for the turbulent layer l, and $\sigma_\phi^{2,l} = \beta_l\sigma_\phi^2$ is the turbulence variance for layer l, where the weights β_l are given by the C_n^2 normalized profile and satisfy

$$\sum_{l=1}^{n_L}\beta_l = 1. \tag{21}$$

This MAP estimation uses only points that belong to the intersection $\mathcal{K}(i, j) \cap \mathcal{P}$ of width r (see Fig. 3). As point f is the furthest point from $\mathcal{P}$, located on one of the main diagonals due to the pixelized square geometry of the convolution kernel h, it exhibits the slowest convergence of $Q_f(r)$ compared with other points in $\mathcal{E}$, when r increases.

Note that both $\sigma_\phi^{2,l}$ and $\sigma_{\tilde{f}}^{2,l}$ depend linearly on β_l and $r_0^{-5/3}$, so that $Q_f(r)$ is independent from the turbulence C_n^2 profile. Therefore, the criterion $Q_f(r)$ does not depend on l, and can be rewritten as

$$Q_f(r) = \frac{1}{\sigma_\phi^2}\text{Cov}(\phi_f, \phi^{\mathcal{P}\cap\mathcal{K}})\text{Var}(\phi^{\mathcal{P}\cap\mathcal{K}})^{-1}\text{Cov}(\phi_f, \phi^{\mathcal{P}\cap\mathcal{K}})^{\text{T}}, \tag{22}$$

where $\text{Cov}(\phi_f, \phi^{\mathcal{P}\cap\mathcal{K}})$ is the cross-covariance matrix of ϕ_f and $\phi^{\mathcal{P}\cap\mathcal{K}}$, and $\text{Var}(\phi^{\mathcal{P}\cap\mathcal{K}})$ is the variance matrix of $\phi^{\mathcal{P}\cap\mathcal{K}}$. As Q_f does not depend on the C_n^2 profile, it can be computed directly from C_ϕ and r for a given value of the outer scale L_0. We choose to set the value of r according to
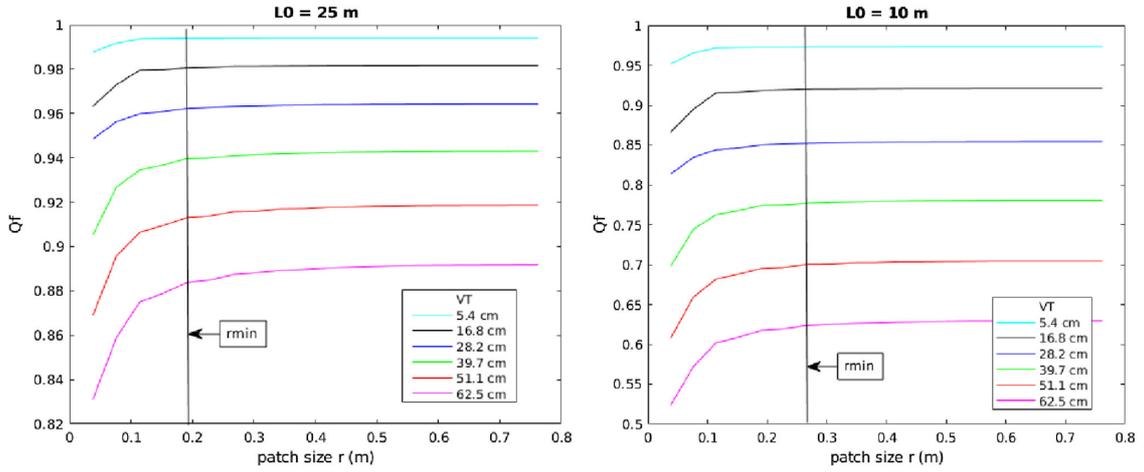
Fig. 4. Convergence of Q_f (and thus of the MAP estimator) for points estimated outside the telescope pupil, for two outer scales $L_0 = 25$ m (left) and $L_0 = 10$ m (right). Values of VT (phase translation norm for one AO frame) range from 5.4 cm to 62.5 cm. The worst value of r_{min} is 19 cm for $L_0 = 25$ m and 26.7 cm for $L_0 = 10$ m.

$$r_{min} = \{ \min(r) | Q_f(r) > 0.995 \, Q_f(D) \}, \qquad \textbf{(23)}$$

with D the telescope diameter. This means that the maximum loss on criterion Q_f is of 0.5% with respect to taking all the points in D. Figure 4 illustrates the behavior of Q_f as a function of r for two outer scales ($L_0 = 25$ m and $L_0 = 10$ m) and different values of VT (wind speed times sampling period). The values chosen for VT represent the turbulent phase translation in one AO frame from astronomy cases (low values below 30 cm), to high altitude layers in LEO satellites tracking cases (high values close to 60 cm).

The estimation error variance $\sigma_{\tilde{f}}^{2,l}$ increases when L_0 decreases, so that Q_f decreases with L_0. However, the variation of convergence speed of $Q_f(r)$ toward its final value $Q_f(D)$ is negligible. The MAP estimation can thus be forced to be spatially well localized, leading to a highly parallelizable structure. It can be compared to results obtained in [42] for phase screens generation, where the MAP estimation needed only two columns (25 cm) of the previous turbulent phase screen (8 m sampled by 64×64 pixels) to ensure spatial statistics consistent with theoretical values.

Matrices A_{Tel} and A_{Edge} in Eq. (18) depend on the wind direction through the kernel h [see Eqs. (10) and (11)]. The complete dynamical model, describing the n_L-layer turbulent volume $\phi_k^{Tel} = \sum_{l=1}^{n_L} \phi_k^{Tel,l}$ is obtained by concatenation of all single layer models,

$$
\begin{pmatrix} \phi_{k+1}^{Tel,1} \\ \vdots \\ \phi_{k+1}^{Tel,n_L} \end{pmatrix} = \begin{pmatrix} A^{(1)} & 0 & 0 \\ 0 & \ddots & 0 \\ 0 & 0 & A^{(n_L)} \end{pmatrix} \begin{pmatrix} \phi_k^{Tel,1} \\ \vdots \\ \phi_k^{Tel,n_L} \end{pmatrix} + \begin{pmatrix} v_k^1 \\ \vdots \\ v_k^{n_L} \end{pmatrix},
$$
$$\textbf{(24)}$$

where the matrices $A^{(l)}$ have a covariance matrix defined according to the single layer model in Eq. (12) or Eq. (18); note that the superscript l indicates the layer number with v^l if v is a vector, and $M^{(l)}$ if M is a matrix. The mutually independent white

noises $\{v^l\}$ are defined similarly to Eq. (19), but they account for the layer dynamics through $A^{(l)}$ leading to

$$\Sigma_v^{(l)} = E(v_k^l (v_k^l)^T) = \beta_l \left(\Sigma_\phi - A^{(l)} \Sigma_\phi (A^{(l)})^T \right). \qquad \textbf{(25)}$$

Note that in our formulation we consider a modified covariance matrix computed with a reduced number of points according to criterion in Eq. (20), instead of a MAP estimation based on the full telescope pupil. This approach differs from the optimal AR1 used in the SCAO mode in [38] and from the Explicit LQG in [25]. As for the multilayer model MCAO model in [24], the authors use a basis spline and the full pupil to compute the matrices $A^{(l)}$.

D. Measurement Models

Assuming a linear wavefront sensor and an integration time of one frame on the WFS camera (see Fig. 1), the closed-loop measurement equation would be

$$y_k = D\phi_{k-1}^{res} + w_k = D\phi_{k-1}^{Tel} + w_k - M_{int} u_{k-2}, \qquad \textbf{(26)}$$

where D is the WFS matrix, $\{w\}$ is a Gaussian white noise with a known covariance matrix Σ_w, and $\phi_k^{res} = \phi_k^{Tel} - N u_{k-1}$. However, as the Kalman gain L_∞ computation does not depend on the command values, we only need to describe the open-loop measurement model y_k^{OL}:

$$y_k^{OL} = D\phi_{k-1}^{Tel} + w_k. \qquad \textbf{(27)}$$

The matrix D must be adapted to the sampling grid chosen for the phase representation in the state-space model. As an example, the case of a Shack–Hartmann WFS with a phase sampling grid three times finer than the WFS grid is illustrated in Fig. 5.

The operations modeled by D simply consist of taking the difference of the average values along the subaperture edges using Simpson weights, based on a Fried geometry. It can be described using the stencils w_x and w_y for the x- or y-slopes:
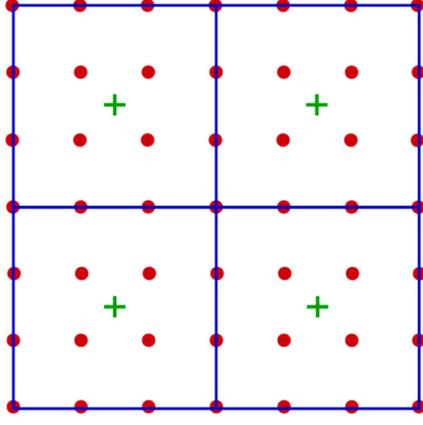
Fig. 5. Measurement model in the case of a Shack–Hartmann WFS where the phase sampling grid of the model is three times finer than the WFS resolution. Four subapertures are represented with blue lines. Phase points are indicated by red points, and slope measurements by green crosses. All 16 phase points of a subaperture are used to compute one measurement.

$$w_x = \frac{1}{d} \begin{bmatrix} -\frac{1}{6} & 0 & 0 & \frac{1}{6} \\ -\frac{1}{3} & 0 & 0 & \frac{1}{3} \\ -\frac{1}{3} & 0 & 0 & \frac{1}{3} \\ -\frac{1}{6} & 0 & 0 & \frac{1}{6} \end{bmatrix}, \qquad w_y = -w_x^{\mathrm{T}}, \qquad \textbf{(28)}$$

where d is the subaperture diameter. Matrix D is then built directly from the values given for w_x and w_y so that the matrix multiply corresponds to the stencil operation.

When a spatially invariant operator is used for perturbation and system modeling, as for example, for the distributed Kalman filter (DKF) in [44], phase samples and measurements must be at the same resolution. A convolution operator h_{wfs} is used instead of a matrix multiply, leading to the measurement model,

$$y_k^{\mathrm{OL}} = h_{\mathrm{wfs}} * \phi_{k-1} + w_k, \qquad \textbf{(29)}$$

where $\phi_{k-1} = \sum_{l=1}^{n_{\mathrm{L}}} \phi_{k-1}^l$. A measurement model with oversampled measurements and phases can then be written in the telescope pupil in matrix form, as

$$y_k^{\mathrm{OL}} = D^{\mathrm{OS}} \phi_{k-1}^{\mathrm{Tel}} + w_k, \qquad \textbf{(30)}$$

where D^{OS} represents the operator that computes oversampled measurements from oversampled phases.

A model error analysis of LQG control design with dynamical and measurement models from Sections 2.B to 2.D will be studied in Section 3.C.

# 3. FIRST PERFORMANCE EVALUATION WITH ZONAL-BASED LQG REGULATORS

A. Simulation Parameters and Setup

Simulations are conducted with the object-oriented MATLAB adaptive optics (OOMAO) simulator in a VLT-NAOS-like case. We consider a science camera image wavelength at $\lambda_{\mathrm{science}} = 1.654\,\mu\mathrm{m}$ and a WFS analysis wavelength at $\lambda_{\mathrm{wfs}} = 0.55\,\mu\mathrm{m}$. The values are gathered in Table 1.

Table 1.   VLT-NAOS-Like AO Parameters

Diameter	8 m
Central occultation	1 m
DM cartesian grid (Fried geometry)	15×15 actuators with 185 valid Gaussian influence function Coupling factor 0.3
Shack–Hartmann (squared subaperture grid)	14×14 sub-apertures with 152 valid
AO loop frequency	500 Hz
λ_{wfs}	$0.55\,\mu\mathrm{m}$
$\lambda_{\mathrm{science}}$	$1.654\,\mu\mathrm{m}$

Table 2.   Pseudo-Boiling Atmosphere Dynamical Parameters for End-to-End Simulations[a]

Layer	3	1
Fractional C_n^2 energy	[0.5, 0.2, 0.3]	1
Wind speed (m/s)	[7.5, 12, 15]	10
Wind direction (°)	[0,120,240]	0
Turbulence configuration		
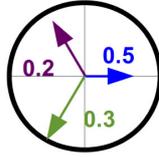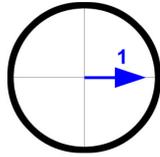
[a]Blue corresponds to the first layer, green to the second layer, and purple to the third layer.

We select a middle range turbulence condition, with $r_0 = 10$ cm cm at 0.55 µm and an outer scale of $L_0 = 25$ m. In this section, two turbulence configurations are considered: a pseudo-boiling resultant turbulence, and a frozen flow turbulence, with the parameters given in Table 2. Note that in all cases, each turbulent layer has a pure frozen flow behavior. For the pseudo-boiling case, we consider a three-layer atmosphere with wind profile, directions, and layers energy giving a resultant turbulent perturbation in the telescope pupil with a behavior very close to boiling. A graphical representation of each wind direction and speed is also proposed in Table 2, where the arrow lengths are proportional to the wind speed and represented on a 15 m/s circle radius, arrow directions are winds directions, and a fractional energy coefficient is written for each arrow.

In this paper, closed-loop performance is evaluated in terms of the Strehl ratio at the science camera wavelength, using the Maréchal approximation,

$$SR = \exp(-\sigma_{\phi^{\mathrm{res}}}^2), \qquad \textbf{(31)}$$

where $\sigma_{\phi^{\mathrm{res}}}^2$ is the residual phase variance in the telescope pupil computed from 15000 phase occurrences of the AO loop. This ensures a numerical accuracy under 0.05 point of the Strehl ratio at the science camera wavelength.

B. Zonal Basis Sampling Choice

Zonal LQG regulators are, of course, affected by the spatial sampling of the turbulent phase model and by the phase interpolation needed when projecting the phase on the DM space to compute the commands through Eq. (2). The interpolation has been systematically done to correspond to the fine sampling

Table 3. **Strehl Ratio at 1.654 μm of Zonal-Based LQG Regulator with a Boiling AR1 Dynamical Model, Using Different Sampling of the Zonal Basis**

Linear sampling (points/actuator pitch)	1	2	3	4
LQG-KF AR1 boiling	42.2%	50.9%	51.7%	52.1%

of the influence functions. We have tested linear and nearest interpolation, which gave similar results, so we have chosen the nearest interpolation. As for the spatial sampling of the turbulent phase model, its effect on the closed-loop control performance can be studied with a simple dynamical model without edge effects: We use a simple dynamical model in the form $\phi_{k+1}^{\text{Tel}} = \alpha \phi_k^{\text{Tel}} + v_k$, where $\alpha < 1$ and associated with the standard measurement model in Eq. (27). This zonal LQG regulator will be called LQG-KF AR1 boiling. The spatial sampling ranges from one to four linear points estimated per actuator pitch (distance between two neighbored actuators); that is, from four to 16 points per subaperture.

As shown in Table 3, the performance increases very fast between one and two linear points per pitch, probably due to the ability of the model to represent a large part of the spatial frequencies that can be generated by the DM. We can deduce from that result that a sampling higher than two linear points per pitch mainly reduces the WFS aliasing, which is similar to LQG regulators when increasing the size of the Zernike modal basis (see [12,45]). We will thus select a minimum linear phase sampling of two points per pitch to analyze the closed-loop performance of zonal-based LQG regulators.

C. AO Model Impact on LQG Regulator Performance

The purpose of this section is to evaluate the performance of the DKF-based LQG regulator and the impact of edge errors for zonal models. To do so, we need to evaluate the impact of the different error sources, thanks to models that are built using different hypotheses. We thus consider several combinations of n_L-layer turbulence dynamical models and measurement models from Sections 2.B to 2.D for the LQG regulators summarized in Table 4. The oversampling is two linear points per actuator pitch, as proposed in the previous section. For the WFS model, the oversampling is done by measurement duplication, as in [26].

We study the three main sources of model errors identified hereafter. Table 5 gathers the performance of regulators [labeled (a)–(d) in the table] in terms of the Strehl ratio for a single frozen flow layer.

The first source of model error is the measurement model error when the measurement model resolution is higher than the real WFS. To evaluate this, (b) and (c) in Table 5 are compared as the only modification between them is that the WFS model is oversampled in (b). It is the main performance loss with 7.4 SR points. In SCAO, using oversampled LQG-DKF is therefore not a good solution. This result is contrary to the MCAO case [26], where measurements better span the telescope pupil.

The second source of model error is the phase model edge error, present with the spatially invariant dynamical model, but also present with the localized dynamical model such as Eq. (12)

Table 4. **Zonal LQG Regulators According to Associated Models**[a, b]

	Regulator Names	Associated Models
(a)	LQG-DKF multilayer AR1	$\phi_{k+1}^l = \alpha h^l * \phi_k^l + v_k^l$ $y_k^{\text{OL}} = h_{\text{wfs}} * \phi_{k-1} + w_k$
(b)	LQG-KF multilayer AR1 OS	$\phi_{k+1}^{\text{Tel},l} = A_{\text{Tel}}^{(l)} \phi_k^{\text{Tel}} + v_k^l$ $y_k^{\text{OL}} = D^{\text{OS}} \phi_{k-1}^{\text{Tel}} + w_k$
(c)	LQG-KF multilayer AR1	$\phi_{k+1}^{\text{Tel},l} = A_{\text{Tel}}^{(l)} \phi_k^{\text{Tel},l} + v_k^l$ $y_k^{\text{OL}} = D \phi_{k-1}^{\text{Tel}} + w_k$
(d)	LQG-KF + MAP multilayer AR1	$\phi_{k+1}^{\text{Tel},l} =$ $(A_{\text{Tel}}^{(l)} + A_{\text{Edge}}^{(l)} M_{\text{MAP}}) \phi_k^{\text{Tel},l} + v_k^l$ $y_k^{\text{OL}} = D \phi_{k-1}^{\text{Tel}} + w_k$

[a]All turbulence models are of AR1 type in each layer, oversampling is two linear points per actuator.
[b]To ease reading of the table, here are a few short descriptions:
(a): spatially invariant models based on convolution kernels (that is, the DKF case based on the infinite pupil hypothesis) where the coefficient $\alpha < 1$ insures stability;
(b): same oversampling for phase and measurements in matrix form (finite pupil) and without edge compensation;
(c): any sampling of the phase, but non-oversampled measurements, in matrix form (finite pupil) without edge compensation; and
(d): any sampling of the phase, but non-oversampled measurements, in matrix form (finite pupil) with edge compensation using MAP estimation.

without MAP edge compensation. By comparing (a)–(c) to (d), we can see that a localized phase dynamical model without MAP compensation for the pupil edge leads to a loss greater or equal to 4.6 SR points.

The last source of model error is the measurement model edge error, when a spatially invariant measurement model is used, although WFS measurements are localized in the telescope pupil. The corresponding loss is evaluated by comparing (a) with (b), and the loss is only 1.2 SR points.

We can deduce from these results that a spatially invariant LQG-DKF regulator is not appropriate for AO systems of the VLT-NAOS type. Moreover, the best results are obtained with a localized measurement model at WFS resolution, and with MAP compensation in the localized dynamical phase model. It is therefore a regulator that will be considered in the rest of the article. This regulator features a multilayer reconstruction with priors on wind profile (speeds and directions) and on the C_n^2 profile. Although this kind of modeling has been shown to improve performance in wide field AO [24,40], computational complexity is an issue even in SCAO, especially when the number of reconstructed layers increases. Indeed, the offline computational complexity of the Riccati equation grows with $\mathcal{O}(n_L^3)$, where n_L is the number of reconstructed layers, and the online prediction equation of the Kalman filter in Eq. (6) grows with $\mathcal{O}(n_L^2)$. An appealing strategy to reduce computational complexity while controlling performance degradation is to design resultant dynamical models in the telescope pupil, which is the topic of the next section.

4. AUTO-REGRESSIVE RESULTANT DYNAMICAL MODELS

This section builds on the works of [24,25,29]. We propose zonal AR1 and AR2 models in SCAO instead of wide-field AO

Table 5. Strehl Ratio at 1.654 μm of Zonal-Based LQG Regulators with Spatially Invariant or Localized Dynamical and Measurement Models[a]

	Regulator Names	Measurement Model Edge Error	Measurement Model Interpolation Error	Dynamical Model Edge Error	Performance (Strehl Ratio)
(a)	LQG-DKF multilayer AR1	YES	YES	YES	45.7%
(b)	LQG-KF multilayer AR1 OS	NO	YES	YES	46.9%
(c)	LQG-KF multilayer AR1	NO	NO	YES	54.3%
(d)	LQG-KF + MAP multilayer AR1	NO	NO	FEW	58.9%
	Turbulence configuration				
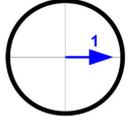
[a]We evaluated the performance with one turbulent layer in frozen flow with a wind of 10 m/s on x-direction.

and propose an easy computation of the transition and covariance matrices. Stability is addressed in Section 4.C. The models are associated with the measurement model in Eq. (27) to obtain the state-space representations gathered in Section 4.D and used to design the LQG regulators. End-to-end performance is evaluated in Sections 5 and 6 through a comparison of many LQG regulators, in Zernike or zonal basis.

A. Resultant Auto-Regressive Model of Order 1 (Lazy SA-LQG)

The SA-LQG in [25,29] corresponds to a resultant AR1 dynamical model with MAP estimation of the points outside the telescope pupil based on all the points inside the telescope pupil, and resorts to bilinear interpolation to estimate the translated phase points. When resorting to bilinear interpolation, the one-step covariance matrix has a simple expression, leading to easy updates of the transition matrix and of the covariance matrix of the process noise v, as shown below.

We briefly present the SA-LQG principle in a SCAO configuration, which is a simplified case of the wide-field AO configuration proposed in [24,25]. The resultant phase in the telescope pupil, ϕ^{pup}, is obtained as the summation of n_{L} turbulent phases $\phi^{\mathrm{Tel},l}$ in the telescope pupil,

$$\phi^{\mathrm{pup}} = \sum_{l=1}^{n_{\mathrm{L}}} \phi^{\mathrm{Tel},l}. \tag{32}$$

The resultant AR1 dynamical model is

$$\phi_{k+1}^{\mathrm{pup}} = A_{\mathrm{pup}} \phi_k^{\mathrm{pup}} + v_k, \tag{33}$$

where the process noise $\{v\}$ is a Gaussian white noise with the appropriate spatial covariance matrix Σ_v. The MAP estimation of ϕ^{pup} knowing ϕ^{Tel} in Section 2.C is applied here in the multilayer case with a given wind profile (speed and directions) and C_n^2 fractional energy distribution. It leads to

$$A_{\mathrm{pup}} = C_\phi^{[1]} \Sigma_\phi^{-1}, \tag{34}$$

where the one-step temporal covariance matrix $C_\phi^{[1]} = E(\phi_{k+1}^{\mathrm{pup}}(\phi_k^{\mathrm{pup}})^{\mathrm{T}})$ of the resultant phase is evaluated with the multilayer model,

$$C_\phi^{[1]} = \sum_{l=1}^{n_{\mathrm{L}}} \mathrm{Cov}(\phi_{k+1}^{\mathrm{Tel},l}, \phi_k^{\mathrm{Tel},l}). \tag{35}$$

Instead of computing $\mathrm{Cov}(\phi_{k+1}^{\mathrm{Tel},l}, \phi_k^{\mathrm{Tel},l})$ in an exact way using the theoretical spatial covariance matrix $C_\phi(\rho)$ in Eq. (14), this one-step temporal covariance matrix is computed from the dynamical model in Eq. (18):

$$\mathrm{Cov}(\phi_{k+1}^{\mathrm{Tel},l}, \phi_k^{\mathrm{Tel},l}) = \beta_l \left(A_{\mathrm{Tel}}^{(l)} + A_{\mathrm{Edge}}^{(l)} M_{\mathrm{MAP}} \right) \Sigma_\phi, \tag{36}$$

where $A_{\mathrm{Tel}}^{(l)}$ and $A_{\mathrm{Edge}}^{(l)}$ are defined in Eq. (11) for each turbulent layer and M_{MAP} is defined in Eq. (17). It is immediately checked that $\mathrm{Cov}(\phi_{k+1}^{\mathrm{Tel},l}, \phi_k^{\mathrm{Tel},l})$ in Eq. (36) can be easily updated when turbulence and wind profiles change: $A_{\mathrm{Tel}}^{(l)}$ and $A_{\mathrm{Edge}}^{(l)}$ are modified according to the wind profile using bilinear interpolations, and the matrix M_{MAP} is modified according to the support defined by r_{min}. From Eq. (36), the transition matrix in each layer is thus $A_{\mathrm{pup}}^{(l)} = \beta_l(A_{\mathrm{Tel}}^{(l)} + A_{\mathrm{Edge}}^{(l)} M_{\mathrm{MAP}})$, so that the resultant transition matrix becomes

$$A_{\mathrm{pup}} = \sum_{l=1}^{n_{\mathrm{L}}} \beta_l \left(A_{\mathrm{Tel}}^{(l)} + A_{\mathrm{Edge}}^{(l)} M_{\mathrm{MAP}} \right), \tag{37}$$

where this expression benefits from the easy updates mentioned above, which is not the case of the global expression used generally under the form $A_{\mathrm{pup}} = C_\phi^{[1]} \Sigma_\phi^{-1}$. Finally, the spatial statistics of $\{v\}$ are adapted to atmospheric turbulence priors through the covariance matrix $\Sigma_v = E(v_k v_k^{\mathrm{T}}) = \Sigma_\phi - A_{\mathrm{pup}} \Sigma_\phi A_{\mathrm{pup}}^{\mathrm{T}}$. The Lazy SA-LQG is the LQG regulator based on the AR1 resultant model defined by the transition matrix in Eq. (37) where the criterion in Eq. (23) is used to limit the number of phase points used for the MAP estimation.

To have a better idea of the sparsity of $A_{\mathrm{pup}}^{(l)}$, sparse and non-sparse matrices are shown in Fig. 6 for one layer in the NAOS-like case used for the simulations in Section 5. The structure of the sparse matrix (Fig. 6, right) is clearly mainly diagonal, and its density (number of nonzero elements divided by total number of matrix elements) is 0.64%. It is less populated than the one shown in [29] (6, middle), where the density of 7.68% as more points are used for the MAP estimation.

As bilinear interpolation is used to compute the translation associated with the dynamical model in Eq. (18), this model will
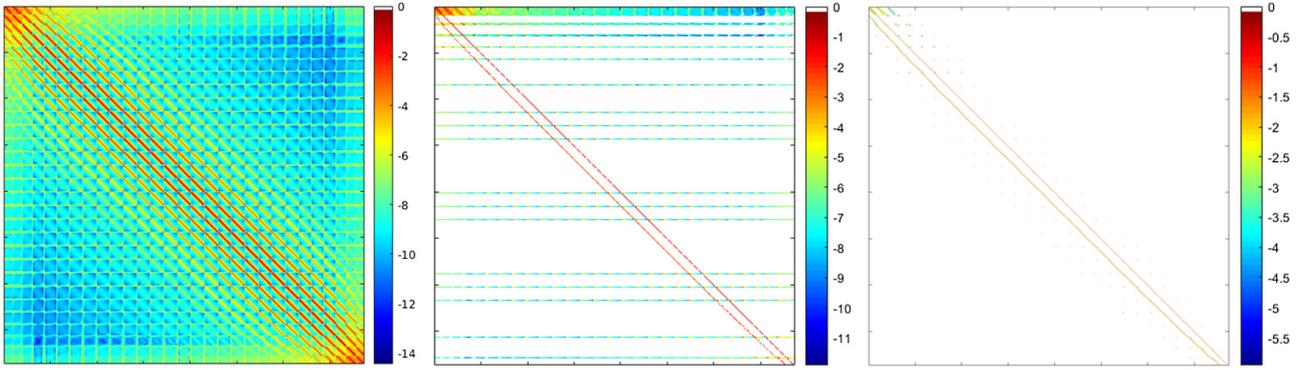
Fig. 6. *A* matrices in the case of a frozen flow atmosphere with a 10 m/s wind speed, $\frac{\pi}{4}$ wind direction, and a 500 Hz loop sampling frequency in logarithmic scale. Left: Matrix *A* for the AR1 model in Eq. (18) build with a MAP estimation on the full telescope pupil, like in the Explicit LQG from [25]. Middle: Corresponding model matrix *A* of the SA-LQG from [29] with a density of 7.68%. Right: Sparse matrix A_pup using a limited number of points according to (23); the density is 0.64%. White corresponds to null values.

---

be marginally stable in the case of an infinite telescope pupil. However, for a finite telescope pupil $\mathcal{P}$, the dynamical model at the telescope edges will affect the stability of Eq. (18) through the update of the phase points that lie inside $\mathcal{P}$. Since a frozen flow prediction using a MAP estimation based on all points in the telescope pupil (like in the Explicit LQG from [25]) is stable (i.e., its spectral radius is strictly less than 1), the modified transition matrix [(Eq. (37) with criterion from Eq. (22) and Eq. (23)] is also a stability matrix. Indeed, it also corresponds to a MAP estimation with respect to a smaller support, so the spectral radius of the corresponding operator is strictly less than 1 also, ensuring the stability of the dynamical model in Eq. (18).

B. Resultant Auto-Regressive Model of Order 2

It is well known that the phase temporal correlation is better represented with an AR2 model than with an AR1 model (see [29,46]). The AR2 model with diagonal matrices A_1 and A_2 has been proposed using either a Zernike basis, as in [14,28], or a zonal basis in [29]. In this section, we do not suppose the matrices to be diagonal anymore and derive from the Yule–Walker equations a fully resultant AR2 model in a SCAO configuration.

The model is defined in the pupil using the same priors (wind and turbulence profiles) as the AR1, and

$$\phi_{k+1}^\text{pup} = A_1 \phi_k^\text{pup} + A_2 \phi_{k-1}^\text{pup} + v_k, \tag{38}$$

where the process noise $\{v\}$ is a Gaussian white noise with the appropriate spatial covariance matrix Σ_v. From the above equation, the matrix-valued Yule–Walker equations are readily obtained as

$$\begin{cases} C_\phi^{[1]} = A_1 \Sigma_\phi + A_2 (C_\phi^{[1]})^\text{T}, \\ C_\phi^{[2]} = A_1 C_\phi^{[1]} + A_2 \Sigma_\phi. \end{cases} \tag{39}$$

The one- and two-step temporal covariance matrices of the resultant phase, respectively, $C_\phi^{[1]} = E(\phi_{k+1}^\text{pup}(\phi_k^\text{pup})^\text{T})$ and $C_\phi^{[2]} = E(\phi_{k+1}^\text{pup}(\phi_{k-1}^\text{pup})^\text{T})$, are computed from a multilayer frozen flow atmosphere model,

$$\begin{cases} C_\phi^{[1]} = \sum_{l=1}^{n_\text{L}} \text{Cov}(\phi_{k+1}^{\text{Tel},l}, \phi_k^{\text{Tel},l}) = \sum_{l=1}^{n_\text{L}} \beta_l C_\phi(\rho - V^l T), \\ C_\phi^{[2]} = \sum_{l=1}^{n_\text{L}} \text{Cov}(\phi_{k+1}^{\text{Tel},l}, \phi_{k-1}^{\text{Tel},l}) = \sum_{l=1}^{n_\text{L}} \beta_l C_\phi(\rho - 2V^l T), \end{cases} \tag{40}$$

with C_ϕ coming from Eq. (14). From Eqs. (39) and (40) we get

$$\begin{cases} A_1 = \left(C_\phi^{[1]} - C_\phi^{[2]} \Sigma_\phi^{-1}(C_\phi^{[1]})^\text{T}\right)\left(\Sigma_\phi - C_\phi^{[1]} \Sigma_\phi^{-1}(C_\phi^{[1]})^\text{T}\right)^{-1}, \\ A_2 = \left(C_\phi^{[2]} - A_1 C_\phi^{[1]}\right)\Sigma_\phi^{-1}. \end{cases} \tag{41}$$

Because Σ_ϕ and $C_\phi^{[1]} \Sigma_\phi^{-1}(C_\phi^{[1]})^\text{T}$ are close, their difference in Eq. (41) cannot be inverted using the approximated covariance matrix in Eq. (36) that was used in the AR1 case. The two matrices A_1 and A_2 will, therefore, be full.

We then choose Σ_v to ensure the proper value of Σ_ϕ:

$$\Sigma_v = \Sigma_\phi - C_\phi^{[1]} A_1^\text{T} - C_\phi^{[2]} A_2^\text{T} - A_1(C_\phi^{[1]})^\text{T}$$
$$+ A_1 \Sigma_\phi A_1^\text{T} + A_1 C_\phi^{[1]} A_2^\text{T} - A_2(C_\phi^{[2]})^\text{T}$$
$$+ A_2 \Sigma_\phi A_2^\text{T} + A_2(C_\phi^{[1]})^\text{T} A_1^\text{T}. \tag{42}$$

Finally, the resultant AR2 model is put in state-space form by taking $X_k = \begin{pmatrix} \phi_k^\text{pup} \\ \phi_{k-1}^\text{pup} \end{pmatrix}$, which leads to

$$\begin{cases} X_{k+1} = \begin{pmatrix} A_1 & A_2 \\ I & 0 \end{pmatrix} X_k + \begin{pmatrix} I \\ 0 \end{pmatrix} v_k, \\ \phi_k^\text{pup} = C_1 X_k, \end{cases} \tag{43}$$

with $C_1 = (I, 0)$.

C. Stability of Resultant Auto-Regressive Dynamical Models

An important property of the resultant AR turbulence models is that they are necessarily stable. In the AR1 case, this stems directly from the fact that the model in Eq. (37) is a weighted sum [see Eq. (21)] of mono-layered and stable dynamical models. The resultant AR1 dynamical model (37) is then obviously stable.

Table 6. Zonal Models with Localized Resultant AR1 and AR2 Dynamical Models and Their Measurement Equation[a,b]

Regulator Names	Associated Models
Lazy SA-LQG (resultant AR1)	$\phi_{k+1}^{\mathrm{pup}} = A_{\mathrm{pup}}\phi_k^{\mathrm{pup}} + v_k.$
	$y_k = D\phi_{k-1}^{\mathrm{pup}} + w_k.$
LQG-KF + MAP (resultant AR2)	$\phi_{k+1}^{\mathrm{pup}} = A_1\phi_k^{\mathrm{pup}} + A_2\phi_k^{\mathrm{pup}} + v_k.$
	$y_k = D\phi_{k-1}^{\mathrm{pup}} + w_k.$

[a] The spatial sampling of the zonal basis used for the turbulent phase model can be chosen independently of the WFS spatial resolution.

[b] The left column gives the labels used for the associated LQG regulators.

For the resultant AR2 model, the state matrix of the dynamical model in Eq. (43), namely,

$$A = \begin{pmatrix} A_1 & A_2 \\ I & 0 \end{pmatrix}, \tag{44}$$

verifies a Lyapunov equation of the form $P = APA^{\mathrm{T}} + Q$, with

$$P = \begin{pmatrix} \Sigma_\phi & C_\phi^{[1]} \\ \left(C_\phi^{[1]}\right)^{\mathrm{T}} & \Sigma_\phi \end{pmatrix}, \quad Q = \begin{pmatrix} \Sigma_v & 0 \\ 0 & 0 \end{pmatrix}. \tag{45}$$

As Σ_ϕ is a covariance matrix with full rank, it is strictly definite positive. It is then immediately checked that, in this case, P is strictly definite positive, Q is semi-definite positive, and the pair $(A, Q^{1/2})$ is controllable. Taken together, these three conditions are sufficient to guarantee that A is a stability matrix, as explained in [47] (Chap. 11, pp. 456–457).

D. Associated Measurement Model

We have defined two new resultant zonal-based models: an easy updatable localized AR1 with a sparse structure and a simplified one-step covariance matrix, and a resultant AR2 dynamical model with a full structure that should hopefully deliver a better performance. They are associated with the measurement model in Eq. (27), where the WFS matrix D is naturally sparse in the zonal basis and easily adaptable to any sampling grid. Expressions are gathered in Table 6. The associated LQG regulators are then readily computed from the corresponding state-space formulations.

## 5. PERFORMANCE ASSESSMENT OF ZONAL LQG REGULATORS: ASTRONOMY CASE

A. Simulation Parameters and Controllers for a VLT-NAOS-Like System

We consider the same AO system configuration as in Section 3.A (Table 1), and we simulate five different turbulence configurations (see Table 7), ranging from a pseudo-boiling to a pure frozen flow turbulent behavior. These different behaviors allow the evaluation of control performance in various configurations of the resulting turbulence and also to discriminate between the candidate regulators.

The multilayer and the AR1 and AR2 resultant LQG regulators developed in this article are built from a zonal model with a sampling of two linear points per actuator pitch (see regulators 7 to 9 in Table 8). It corresponds to a 29×29 Cartesian grid. Six other controllers that have been proposed previously in the literature are also evaluated:

1. The classical integral action controller with global gain $g = 0.6$.
2. A modal LQG regulator based on a boiling AR2 dynamical model, named LQG AR2 boiling, using 495 Zernike modes and similar to the controller that has been successfully implemented on the CANARY demonstrator [14].
3. The LQG AR2 boiling—large, same model as LQG AR2 boiling above, but with 779 Zernike modes.
4. The Frozen LQG multilayer regulator from [23], the first LQG regulator that combines pure frozen flow with a modal basis. The Frozen LQG multilayer includes an estimation step with the AR2 boiling dynamical model of point 2, and a prediction step in a zonal basis using frozen flow assumptions. It is implemented here for a multilayer reconstruction with the best edge compensation proposed in [23] (that is, a filling of the empty crescent with a prediction using the AR2 boiling model).
5. A zonal LQG regulator with a multilayer atmosphere model, tested for wide-field AO in [24] and in [25] where it is called Explicit LQG. The model corresponds to a MAP prediction in each layer using the entire pupil to estimate the predicted phase points. Note that this regulator in SCAO mode needs an additional scalar α coefficient close to 1 in the multilayer dynamical model,

Table 7. Atmosphere Configurations Used in End-to-End Simulations, from Pseudo-Boiling to Frozen Flow Behavior[a,b]

Atmosphere Resultant Behavior	Pseudo-Boiling (3 layers)	Mainly Boiling (3 layers)	Mainly Frozen Flow (3 layers)	Frozen Flow (1 layer)	Frozen Flow (1 layer)
Fractional C_n^2 (%)	[0.5, 0.2, 0.3]	[0.7, 0.1, 0.2]	[0.7, 0.1, 0.2]	1	1
Wind speed (m/s)	[7.5, 12, 15]	[7, 10, 15]	[7, 10, 15]	10	20
Wind direction (°)	[0, 120, 240]	[0, 120, 240]	[0]	0	0
Turbulence configuration					
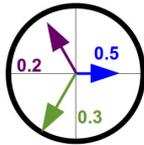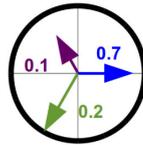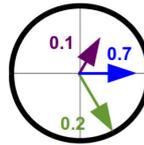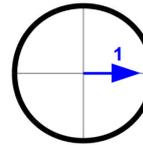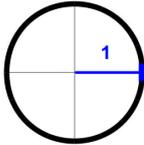
[a] On the graphical representations, blue corresponds to the first layer, green to the second and purple to the third layer.

[b] Only one layer is considered in pure frozen flow configuration.

Table 8. Strehl Ratio at 1.654 μm of Zonal Based LQG Regulators, Compared to a Standard Integral Action Regulator for Five Different Atmosphere Behaviors for a VLT NAOS-Like Case[a]

Controller	State Vector Size	Atmosphere				
		Pseudo-Boiling	Mainly Boiling	Mainly Frozen Flow	Frozen Flow (10 m/s)	Frozen Flow (20 m/s)
1. Integral action $g = 0.6$	185	50.5%	50.6%	50.3%	50.7%	46.4%
2. LQG AR2 boiling from [14], 495 Zernike modes	990	53.7%	53.7%	53.6%	53.8%	51.8%
3. LQG AR2 boiling—large from [14], 779 Zernike modes	1558	54.6%	54.5%	54.4%	54.7%	52.5%
4. Frozen LQG multi-layer from [23], 495 Zernike modes	2970 (multi-layer) 990 (frozen flow)	52.6%	53.4%	54.6%	55.6%	55.6%
5. Explicit LQG from [24,25], 29 × 29 points	2319 (multi-layer) 773 (frozen flow)	55.5%	55.8%	56.5%	58.9%	59.3%
6. SA-LQG from [25,29], 29 × 29 points	773	52.5%	53.6%	55.3%	57.7%	57.4%
7. LQG-KF + MAP multi-layer AR1, Table 4, 29 × 29 points	2319 (multi-layer) 773 (frozen flow)	55.6%	56.0%	56.4%	57.7%	57.4%
8. Lazy SA-LQG (resultant AR1), Table 6, 29 × 29 points	773	52.5%	53.6%	55.3%	57.7%	57.4%
9. LQG-KF + MAP resultant AR2, Table 6, 29 × 29 points	1546	53.8%	54.3%	55.9%	58.9%	59.5%
Turbulence configuration						

[a]The numerical accuracy of the Strehl ratio calculations is under 0.05 point at the science camera wavelength.

$$\phi_{k+1}^{\text{Tel},l} = \alpha A^{(l)} \phi_k^{\text{Tel},l} + v_k^l, \tag{46}$$

where α is chosen between 0.9950 and 1 to ensure best performance, and must be tuned for each turbulence behavior.

6. A zonal LQG regulator with a resultant AR1 dynamical model, the SA-LQG, proposed in a wide-field AO in [25,29].

B. Control Performance Results

No less than a total of nine regulators have been evaluated exactly in the same conditions for the five turbulence configurations described in Table 7. The results are gathered in Table 8.

1. Performance Analysis

The worst performance for all atmosphere configurations is given by the integral action controller (1), which means that all the other regulators benefit from the Kalman filter phase prediction, whatever the model. The best performance is obtained, as expected, by the regulator that is built on the most informative model; that is, the Explicit LQG (5). Its turbulent phase dynamical model is indeed the closest one from the simulated turbulence, with all layers reconstructed using the complete knowledge of wind and turbulence profiles.

The two LQG AR2 boiling regulators (2 & 3) are well adapted to pseudo-boiling and mainly boiling atmosphere configurations, and the increase of Zernike modes in the model

(495 to 779) improves the overall performance as expected. However, their performance in the two frozen flow turbulence configurations (54.7% SR and 52.5% SR) is lower than all the LQG regulators (4–9) that are designed using frozen flow models.

As for the LQG regulators 4 and 7 that are based on a multilayer reconstruction, the Frozen LQG multilayer in Eq. (4) improves performance when the turbulence configuration tends to a frozen flow behavior, but is less interesting than the LQG-KF + MAP multilayer AR1 in Eq. (8), which gives slightly better results for less complexity. (See the state vector size and remember that the LQG-KF + MAP multilayer AR1 has a very sparse state matrix.)

Finally, we analyze the performance of the three LQG regulators based on the resultant models in the pupils 6, 8 and 9. The two SA-LQG regulators 6 and 8 give the worse performance in the pseudo-boiling configuration, with only a 52.5% SR. The approximations made to derive the very sparse model of the Lazy SA-LQG induce no visible performance degradation compared to the SA-LQG. The LQG-KF + MAP resultant AR2 in Eq. (9) gives good average performance in all three-layer turbulence configurations (pseudo-boiling, mainly boiling, and mainly frozen flow columns), and gives excellent performance in the two frozen flow configurations, with 58.9% SR and 59.5% SR. The increase of the model order (from AR1 to AR2) leads, as expected, to an improvement for all turbulence configurations because it allows for a better modeling of the resultant turbulence temporal correlation, as shown below.
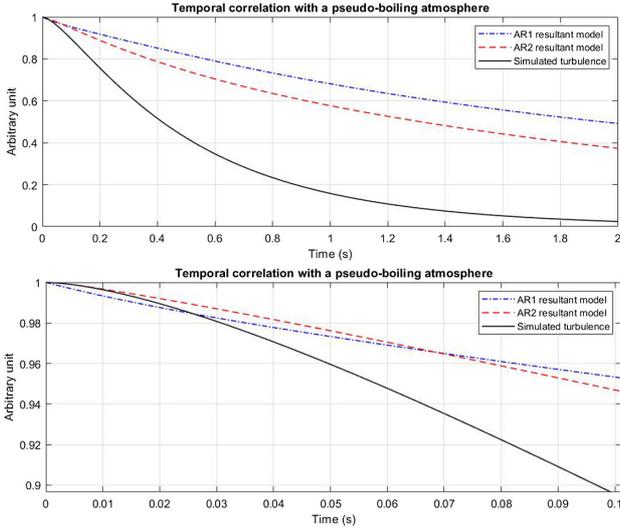
Fig. 7. Top: temporal correlation of one central pixel for AR1 (dotted-dashed) and AR2 (dashed) models compared with true turbulence (plain). Bottom: zoom on 0.1 s.

---

2. AR1 and AR2 Temporal Correlations

The temporal correlations are presented in Fig. 7 to appreciate the different behaviors between the AR1 and the AR2 resultant models.

Figure 7 (top) shows that the AR1 and AR2 models do not fit the true correlation (corresponding to the resultant three-layer turbulence). The zoom on the first 0.1 s in Fig. 7 (bottom) shows why the AR2 model gives better control results: The short-term correlation (time < 0.01 = 5 AO frames) is better represented with the AR2 model, which has a significant impact on the accuracy of the short-term phase prediction $\hat{\phi}_{k+1|k}^{Tel}$ in Eq. (9) given by the Kalman filter.

3. Implementation

We have made all our calculations using MATLAB on a CPU-based computer featuring two processors Xeon E5-2699 V4 (22 cores each, 2.2 to 3.6 GHz, 35 Mb cache) and 512 Gb DDR4 ECC RAM.

For the most demanding regulator (the Frozen LQG multilayer with $n_x = 2070$ state components), less than 50 s were needed to compute the regulator given the C_n^2 and wind profiles (7 s to compute the state model and 40 s to compute the Kalman gain, which includes the resolution of the Riccati equation). For the regulator with best results (Explicit LQG with $n_x = 2319$), about 40 s are needed (5 + 35). The two resultant AR1 and AR2 regulators stay below 4 s and 13 s, respectively. There is, therefore, no problem for the update of such controllers regarding the evolution of atmospheric and wind profiles.

As for real-time implementation, it can be divided into two main parts: the command calculation, and the state and control term updates. The command calculation has exactly the same structure as an integrator equation: $u_k = u + M_1 y_k$, where M_1 is a matrix of dimensions $n_u \times n_y$, n_u being the number of actuators and n_y the number of measurements. This structure is obtained from the update of the regulator using Eqs. (2), (6),

and (9). The state and control term u updates can be separated in different parallel threads according to available memory and hardware, so we only give the number of matrix vector multipliers (MVMs) and their dimensions: There are four MVMs, corresponding to $n_x \times n_x$, $n_x \times n_y$, $n_x \times n_u$, and $n_u \times n_x$ operations. For the Explicit LQG with three layers and an upsampling of 2, $n_x = 2319$ roughly corresponds to 12 times the DM size. For the LQG-KF + MAP resultant AR2 and in the same configuration, $n_x = 1546$ is about eight times the DM size, whereas it is only four times for the Lazy SA-LQG ($n_x = 773$).

C. Performance Robustness of Resultant Models to Errors on Wind Profile

To analyze the robustness of the Lazy SA-LQG and LQG-KF + MAP resultant AR2, several tests have been done with a pseudo-boiling behavior and a mainly frozen flow behavior of the simulated multilayer atmosphere (see Table 7). We consider model errors consistent with wind profile measurements errors of the Stereo-SCIDAR [48] as indicated in [32]. We thus took two cases of wind profiles mismatch:

- weak errors, with a variation range of ±2.5 m/s for the wind speed norm and ±10° for the wind direction; and
- strong errors, with a variation range of ±5 m/s for the wind speed norm and ±20° for the wind direction.

The weak errors case corresponds to the Stereo-SCIDAR resolution on wind norms and directions for the slowest layers that are detected with nonzero speed, as described in [32].

We have applied the maximum error bounds described above to the true profiles (three simulated layers = 4^3 cases), for each weak or strong case in a pseudo-boiling or in a mainly frozen flow atmosphere, which makes $4^3 \times 4 = 256$ profiles combinations. These 256 different profiles have been used to compute the models of the Lazy SA-LQG and the LQG-KF + MAP resultant AR2, leading to 512 end-to-end simulations of 15000 samples each. The results are shown in Table 9 and Fig. 8.

From these results, we can see that the mean loss in performance due to wind profile mismatch is globally limited. We can thus expect a good performance robustness with respect to wind profile errors in various turbulence configurations. It also appears that, according to Table 9, the Lazy SA-LQG is more robust in performance than the LQG-KF + MAP resultant AR2, in particular with strong errors on the wind profile measurements and an atmosphere configuration with a dominant frozen flow behavior. However, better average and min–max results are obtained with the AR2 resultant model, except for the case with frozen flow atmosphere and strong errors on all wind profile values (see Table 9). In this case, a few simulations led to less than 52%, with a worse case at 48%. To limit performance variation, these model-based controllers could be complemented with a real-time characterization of the wind profile, as proposed in [32].

For other applications such as LEO satellite tracking in Section 6, turbulence dynamics are much faster and very high wind speeds due to satellite motion are known with good accuracy, as explained in next section.

Table 9. Performance of the Lazy SA-LQG and LQG-KF + MAP Resultant AR2 Regulators at 1.654 μm without Model Error, and with Weak and Strong Errors on Wind Profiles Priors Used for Model Computations[a, b, c]

Regulator	Atmosphere	No Error	Weak Error ± Std Dev	Strong Error ± Std Dev
Lazy SA-LQG	Pseudo-Boiling	52.5%	52.4% ± 0.1	52.0% ± 0.2
(resultant AR1)	Mainly Frozen Flow	55.3%	55.0% ± 0.2	54.5% ± 0.4
LQG-KF + MAP	Pseudo-Boiling	53.8%	53.5% ± 0.3	52.7% ± 0.6
(resultant AR2)	Mainly Frozen Flow	55.9%	55.2% ± 0.6	53.4% ± 1.8

[a]The value of the standard deviation is also indicated. The numerical accuracy of the Strehl ratio is under 0.05 points at the science camera wavelength.
[b]The two different atmosphere configurations can be found in Table 7.
[c]The linear sampling of the zonal basis is two points per actuator pitch.
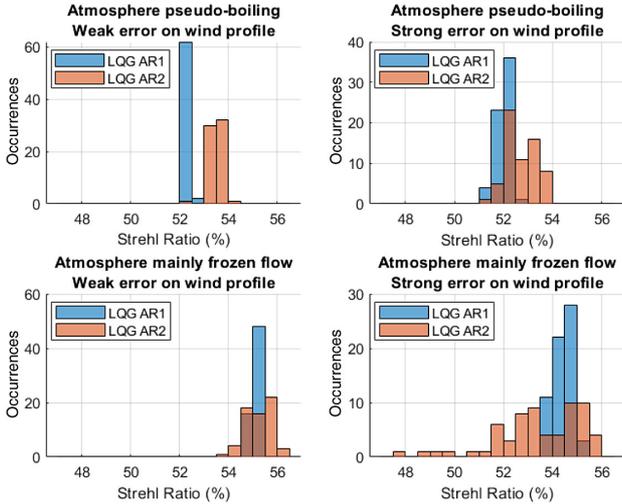

Fig. 8. Histogram of the performance results in four different cases (two different atmosphere and two wind profile error configurations), for AR1 and AR2 LQG regulators (see Table 6). Each bin width is 0.5 point of the Strehl ratio at 1.654 μm. The number of simulated trajectories in each of the four cases is 64.

6. PERFORMANCE ASSESSMENT OF ZONAL LQG REGULATORS: SATELLITE TRACKING CASE

A. Simulation Parameters

We consider here a low earth orbit observation, with a satellite at zenithal coordinates, an altitude of 765 km, and a speed of 7.5 km/s. We take the worst atmospheric condition proposed in [35], namely, a seeing condition of 2", equivalent to $r_0 = 5.67$ cm at 0.55 μm, and an outer scale of $L_0 = 25$ m. In this application the telescope is affected by both the natural behavior of the turbulence layers and the apparent layers translations due to the satellite motion above the telescope. For our end-to-end simulations, we consider a six-layer atmosphere with altitude and fractional energy distribution described in Table 10. The satellite speed induces very high values of the apparent wind norms in altitude and all with the same direction, as they correspond to the projection of the satellite speed on the layers. For the altitude layers (here from two to six), the atmospheric wind is comparatively very low and has been neglected. Only the ground layer keeps its natural atmospheric wind speed, with a 10 m/s norm and a different direction (see Table 10).

Table 10. Atmosphere Parameters for the LEO Satellite Tracking End-to-End Simulations[a, b]

Layers	Fractional C_n^2 Energy (%)	Altitude (km)	Wind Speed (m/s)	Wind Direction (°)
1	0.45	0	10	60
2	0.1	2	19.60	0
3	0.125	5	49.02	0
4	0.125	7	68.63	0
5	0.15	10	98.04	0
6	0.05	12	117.64	0

[a]The C_n^2 profile is adapted from the six-layer atmosphere considered in [35].
[b]Layers two to six have wind speeds that are the projection of the satellite speed on their altitudes.

We simulate a Shack–Hartmann WFS, with a 16×16 subaperture grid (204 valid), and with a measurement noise variance $\sigma_\phi^2 = 0.2$ rad[2] at the edge of the subaperture, at 0.55 μm. The DM has a cartesian grid of 17×17 actuators in a Fried geometry, with 265 valid actuators. The AO loop rate is 2 kHz. The telescope diameter of the primary mirror is 1.8 m, with a central occultation of 20 cm. The WFS guide star is the satellite itself and a geometric Shack–Hartmann model is used for slopes computation. As we compare the performance of different controllers, we do not consider pointing errors of the tracking systems, and therefore assume that the science direction is fixed on the center of the satellite.

B. LQG Control Loop Settings

Closed-loop end-to-end simulations of the LEO satellite tracking case are performed on 15000 iterations, and the results are summarized in Table 11. The performance is evaluated at 800 nm. We keep the same numeration as Table 8, and description of the regulators is in Section 5.A.

The multilayer reconstruction with the LQG-KF + MAP multilayer AR1 from Table 4 has been evaluated with a reconstruction on all six layers or with a reconstruction on less than six layers, using for each resultant layer the modeling defined for the Lazy SA-LQG in Eq. (37) to reduce the computational complexity. The wind speed norm V_{eq} of a resultant layer is then computed according to

$$V_{\text{eq}} = \left(\frac{\sum_{l=n_1}^{n_l} \beta_l (V^l)^{5/3}}{\sum_{l=n_1}^{n_l} \beta_l} \right)^{3/5}, \tag{47}$$

Table 11. Strehl Ratio at 800 nm for Several LQG Regulators with Zonal or Modal Basis Dynamical Models Compared to a Standard Integral Action Regulator[a]

Controller	State Vector Size	Strehl Ratio at 0.8 µm
1. Integral action $g = 0.55$	265	10.4%
8. Lazy SA-LQG (Table 6), 33×33 points	989	27.2%
6. SA-LQG from [29], 33×33 points	989	28.3%
2. LQG AR2 boiling from [14], 495 Zernike modes	990	29.0%
4. Frozen LQG multi-layer from [23], 495 Zernike modes	5940	39.5%
7. LQG-KF + MAP 2-layer AR1 Table 4), 33×33 points	1978	46.0%
9. LQG-KF + MAP resultant AR2 (Table 6), 33×33 points	1978	50.1%
7. LQG-KF + MAP 4-layer AR1 (Table 4), 33×33 points	3956	51.6%
7. LQG-KF + MAP 6-layer AR1 (Table 4), 33×33 points	5934	51.9%
5. Explicit LQG from [24], 33×33 points	5934	53.2%

[a]The LEO tracking atmosphere behavior is described in Table 10.

Table 12. Atmosphere Parameter for Zonal LQG Regulators with a Multilayer Reconstruction with a Reduced Number of Layers[a]

Controller	Fractional C_n^2 Energy (%)	Wind Speed (m/s)	Wind Direction (°)
LQG-KF + MAP 2-layer AR1	[0.45, 0.55]	[10, 72.54]	[60, 0]
LQG-KF + MAP 4-layer AR1	[0.45, 0.1, 0.25, 0.2]	[10, 19.60, 59.37, 103.18]	[60, 0, 0, 0]

[a]The wind speeds and the C_n^2 profiles are computed with the atmosphere parameters from Table 10.

which is similar to the astronomy case [49], and where $\{n_1, \ldots, n_l\}$ are the indexes of the layers with same wind direction to be concatenated in the model. We chose to take into account either two or four layers in the multilayer models to reduce the complexity with atmosphere parameters and wind profiles defined in Table 12.

C. Performance Results and Analysis

As expected, the multilayered zonal LQG regulators give very good performance. The Zernike LQG AR2 boiling regulator is close to a 30% Strehl ratio, giving much better results than the standard integral action controller. The latter performs poorly due to the bad seeing conditions and very fast dynamics of the perturbation. The Frozen LQG multilayer significantly improves the performance with respect to the LQG AR2 boiling in Zernike basis, but is much heavier in terms of computational complexity.
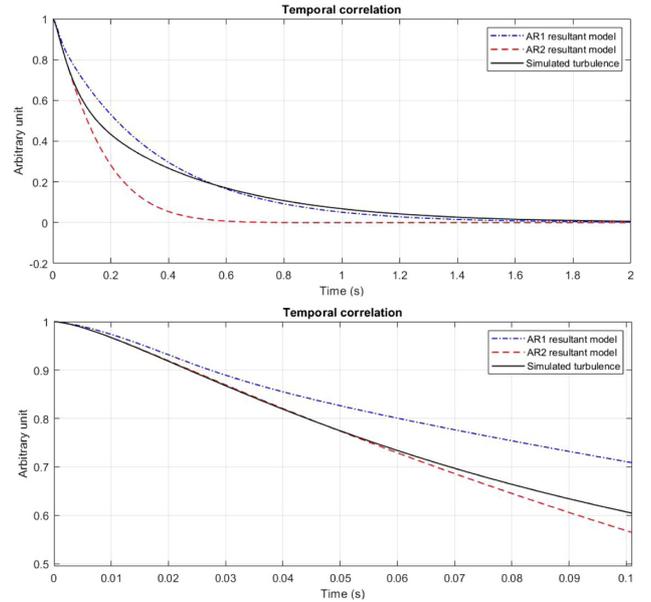

Fig. 9. Top: temporal correlation of one central pixel for AR1 (dotted-dashed) and AR2 (dashed) resultant models compared with true turbulence (plain). Bottom: zoom on 0.1 s.

From this point of view, the implementation of the 4, 5, and 7 regulators with a six-layer reconstruction and large state vectors may benefit from the latest developments in high-performance computing for tomographic AO (see, e.g., [50,51]). It can be noted that the approximations in regulator 7 (the six-layer LQG-KF + MAP multilayer AR1 with truncated MAP estimation and bilinear interpolation) lead to limited performance loss when compared with Explicit LQG. The latter gives the best results with a 53.2% of Strehl ratio. It is also almost the most demanding one with $n_x = 5934$ state components, leading to approximately 316 s to compute the regulator (16 s for the state model and 300 s for the Kalman gain). Considering the discussion on complexity in Section 5.B.3, it would be interesting to further study its challenging real-time implementation at 2 kHz.

The Lazy SA-LQG, SA-LQG, and LQG AR2 boiling have similar performance, so that the LQG AR2 boiling stays very attractive with its low-size state vector (leading to less than 5 s for the offline calculations) and ease of use.

At last, the best compromise is obtained by the LQG-KF + MAP resultant AR2 with a 50.1% Strehl ratio and a limited state vector size of $n_x = 1978$, so that only 20 s are needed (6 s + 14 s) for the offline calculations. This regulator should not be too difficult to implement for real-time operations and thus seems perfectly adapted to this LEO satellite tracking application. Indeed, the priors used to compute its dynamical model are reliable because the value of the satellite speed is known with good accuracy. With such a level of performance, the hardware constraints could be relaxed to improve the SNR by lowering the frequency rate and thereby the measurement noise.

In terms of temporal covariance behavior, it can be seen that even though the AR1 model seems to give a correlation closer to the true average turbulence in Fig. 9 (top), it is clear in Fig. 9 (bottom) that the short-term correlation is much better
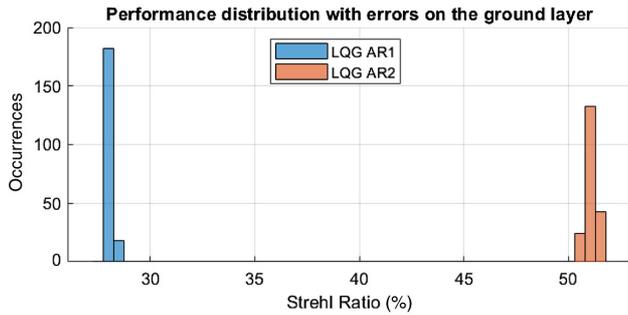
Fig. 10. Histogram of the performance results for the LQG regulators based on AR1 (Lazy SA-LQG) and AR2 (LQG-KF + MAP resultant AR2) resultant models (see Table 6). Each bin width is 0.5 point of Strehl ratio at 800 nm. The number of simulated trajectories for each model is 200.
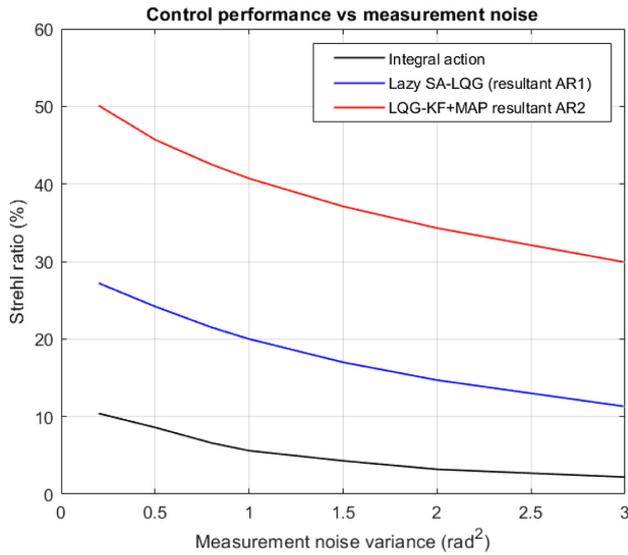

Fig. 11. Strehl ratio at 0.8 μm of Lazy SA-LQG and LQG-KF + MAP resultant AR2, compared with a standard integral action controller for seven different values of the WFS measurement noise variance. The numerical accuracy of the Strehl ratio calculations is under 0.05 point at the science camera wavelength.

represented with the AR2. This largely explains the significant performance improvement brought by the LQG-KF + MAP resultant AR2 over the Lazy SA-LQG and the SA-LQG (which behave similarly).

Performance histograms for the LQG regulators based on the AR1 and AR2 resultant models are shown in Fig. 10. Errors on wind speed and direction of the natural wind (first layer only) are taken uniformly over $[-2.5, 2.5]$ m/s and $[-10, 10]$ degrees, respectively. Results show a very good performance robustness with less than two points of Strehl ratio variation.

To further analyze the performance with different WFS measurement noise variances, simulations have been conducted with a range of variance values from 0.2 rad^2 to 3 rad^2 at the edge of the subaperture, at 0.55 μm. The results are displayed in Fig. 11, which helps us appreciate the performance robustness with the increasing values of the measurement noise variance.

The gain of the integral action controller was not best-tuned because its performance is too poor. It stays below 10% of Strehl ratio for a measurement noise variance greater than 0.5 rad^2. The Lazy SA-LQG stays roughly at 20 points under the LQG-KF + MAP resultant AR2. It therefore appears not as well adapted as the LQG-KF + MAP resultant AR2 regulator, which remains above 30% of Strehl ratio, even for a large measurement noise variance value of 3 rad^2, and above 40% of Strehl ratio for a measurement noise variance of 1 rad^2 or less. Considering the high sampling AO loop rates usually used for space situational awareness (SSA) applications, the DM's dynamics may become non-negligible as the AO sampling frequency increases. As mentioned in Section 2.A, they can be accounted for in the design using standard control tools.

7. CONCLUSION

In this article we investigate LQG AO control with zonal turbulence models based on the frozen flow hypothesis for VLT-type systems in a SCAO configuration and for a LEO satellite tracking-type AO system. We propose a localized edge compensation mechanism consisting of an offline MAP estimation with reduced support, which leads to a sparser state matrix in the turbulence state models (a 0.64% density in our example). The support is defined by selecting a set of phase points so that less than 0.5% of the normalized estimation error variance is lost with respect to taking all the phase points inside the telescope pupil. We show that this change does not lead to any significant performance degradation. Based on a VLT-NAOS-type configuration, we first test the DKF [44] that appears to gives disappointing performance results. To understand the reason for this low performance, we identify the impact of the different approximations affecting zonal-based regulators, from the spatially invariant DKF (infinite pupil hypothesis) to a multilayer dynamical model with finite pupil. We show that the DFK measurement model has a major impact on this performance degradation.

We then propose to design turbulence dynamical models that are resultant in the pupil, based on turbulence and wind profiles priors. This approach is similar to [24,25,29], where AR1 models are proposed for LQG regulators. Using the reduced support for MAP estimation and a simplification of the one-step covariance matrix calculation in the Yule–Walker equation resolution, we derive the Lazy SA-LQG, an AR1 model close to the zonal SA-LQG in [29]. A new AR2 resultant model (LQG-KF + MAP resultant AR2) is also proposed with full regression matrices. Note that these resultant regulators can be built using any number of layers without modifying their final dimensions.

No less than eight LQG regulators based on different modeling assumptions are then evaluated and compared with the integrator for an AO system in a VLT-NAOS-like case with an average seeing condition and good SNR. Performance results are compared, in particular with the regulator used on sky in [52], with the Explicit LQG in [25], and with the SA-LQG in [29]. Five different multilayer atmosphere configurations are simulated, from a quasi-boiling resultant atmosphere to a quasi-pure and pure frozen flow atmosphere. Among all the LQG regulators using resultant models, the LQG-KF + MAP resultant AR2 gives the best results, in particular when the

atmosphere is of the quasi-pure or pure frozen flow type. An analysis of model behavior through temporal covariances shows the AR2 resultant model is much more accurate for short-term covariance values, leading to a better phase prediction. As for robustness with respect to wind profile errors, we show that performance loss is globally limited, with a stronger robustness for AR1 models. Typical errors on wind profiles have been chosen from the Stereo-SCIDAR accuracy values in [32].

The LEO satellite tracking case starts with an integrator that gives about 10% of Strehl ratio. We show that a 50% Strehl ratio can be obtained with the LQG-KF + MAP resultant AR2, which exhibits the best compromise in terms of computational complexity. Similar to the astronomical case, model behaviors are analyzed through their temporal covariances, and a study with respect to wind value errors of the ground layer shows a good robustness of the control performance. In addition, performance assessment has been conducted under average or poor SNR conditions, showing that performance improvement stays high. It is clear that the predictive capabilities of these zonal LQG regulators take advantage of the quasi-pure frozen flow behavior of the altitude layers. Several simplifying hypothesis have been considered in our simulations. First, several layers close to the ground (and not only the ground layer) could have their own wind speed in addition to the apparent tracking speed due to the telescope motion. Second, interframe motion is not considered in our simulations, and the satellite motion during the WFS exposure time would probably lead to an increase in the measurement noise. Third, as the satellite is an extended source, the WFS measurement model should rely on intercor-relation of subaperture images, instead of using a natural guide star with a geometric WFS model. Finally, among the many additional sources of errors that could be accounted for when simulating a complete system, scintillation effects may strongly affect performance in the satellite case, as in [53], but is beyond the scope of this paper. However, considering the large perform-ance gap between the regulators, accounting for these effects should still allow for a significant performance improvement. Implementation in a real system, besides being obviously of great interest, would probably also require some model adjust-ments. It is, for example, possible to mix boiling and frozen flow behaviors by combining several models, such as a boiling AR2 Zernike model with an AR2 resultant zonal model based on the frozen flow hypothesis. Real experimentation would allow even further development of the zonal models presented here, which would be a natural extension of this work.

REFERENCES

1. F. Roddier, *Adaptive Optics in Astronomy* (Cambridge, 1999).
2. B. Macintosh, J. Graham, D. Palmer, R. Doyon, D. Gavel, J. Larkin, B. Oppenheimer, L. Saddlemyer, J. K. Wallace, B. Bauman, D. Erikson, L. Poyneer, A. Sivaramakrishnan, R. Soummer, and J.-P. Veran, "Adaptive optics for direct detection of extrasolar planets: the Gemini planet imager," C. R. Phys. **8**, 365–373 (2007).
3. T. Fusco, C. Petit, G. Rousset, J.-F. Sauvage, K. Dohlen, D. Mouillet, J. Charton, P. Baudoz, M. Kasper, E. Fedrigo, P. Rabou, P. Feautrier, M. Downing, P. Gigan, J.-M. Conan, J.-L. Beuzit, N. Hubin, F. Wildi, and P. Puget, "Design of the extreme AO system for SPHERE, the planet finder instrument of the VLT," Proc. SPIE **6272**, 62720K (2006).
4. P. Kern, P. Léna, P. Gigan, J.-C. Fontanella, G. Rousset, F. Merkle, and J.-P. Gaffard, "COME-ON: an adaptive optics prototype dedicated to infrared astronomy," Proc. SPIE **1130**, 54–64 (1989).
5. G. Rousset, J. Fontanella, P. Kern, P. Gigan, and F. Rigaut, "First diffraction-limited astronomical images with adaptive optics," Astron. Astrophys. **230**, L29–L32 (1990).
6. R. N. Paschall and D. J. Anderson, "Linear quadratic Gaussian control of a deformable mirror adaptive optics system with time-delayed measurements," Appl. Opt. **32**, 6347–6358 (1993).
7. C. Dessenne, P.-Y. Madec, and G. Rousset, "Optimization of a predic-tive controller for closed-loop adaptive optics," Appl. Opt. **37**, 4623–4633 (1998).
8. C. Dessenne, P.-Y. Madec, and G. Rousset, "Sky implementation of modal predictive control in adaptive optics," Opt. Lett. **24**, 339–341 (1999).
9. B. Le Roux, C. Kulcsár, L. M. Mugnier, T. Fusco, H.-F. Raynaud, and J.-M. Conan, "Optimal control law for classical and multiconjugate adaptive optics," J. Opt. Soc. Am. A **21**, 1261–1276 (2004).
10. D. P. Looze, "Linear-quadratic-Gaussian control for adaptive optics systems using a hybrid model," J. Opt. Soc. Am. A **26**, 1–9 (2009).
11. C. Kulcsár, H.-F. Raynaud, C. Petit, J.-M. Conan, and P. V. de Lesegno, "Optimal control, observers and integrators in adaptive optics," Opt. Express **14**, 7464–7476 (2006).
12. C. Kulcsár, H.-F. Raynaud, C. Petit, and J.-M. Conan, "Minimum variance prediction and control for adaptive optics," Automatica **48**, 1939–1954 (2012).
13. G. Sivo, C. Kulcsár, J.-M. Conan, H.-F. Raynaud, E. Gendron, A. Basden, F. Vidal, T. Morris, S. Meimon, C. Petit, D. Gratadour, O. Martin, Z. Hubert, G. Rousset, N. Dipper, G. Talbot, E. Younger, and R. Myers, "First on-sky validation of full LQG control with the CANARY MOAO pathfinder," in *AO4ELT3* (2013).
14. G. Sivo, C. Kulcsár, J.-M. Conan, H.-F. Raynaud, E. Gendron, A. Basden, F. Vidal, T. Morris, S. Meimon, C. Petit, D. Gratadour, O. Martin, Z. Hubert, A. Sevin, D. Perret, F. Chemla, G. Rousset, N. Dipper, G. Talbot, E. Younger, R. Myers, D. Henry, S. Todd, D. Atkinson, C. Dickson, and A. Longmore, "First on-sky SCAO vali-dation of full LQG control with vibration mitigation on the CANARY pathfinder," Opt. Express **22**, 23565–23591 (2014).
15. N. Doelman, R. Fraanje, and R. Den Breeje, "Optimal control of tip-tilt modes on-sky Adaptive Optics demonstration," in *AO4ELT2* (2011).
16. A. Guesalaga, B. Neichel, J. O'Neal, and D. Guzman, "Mitigation of vibrations in adaptive optics by minimization of closed-loop residuals," Opt. Express **21**, 10676–10696 (2013).
17. C. Petit, J.-F. Sauvage, T. Fusco, A. Sevin, M. Suarez, A. Costille, A. Vigan, C. Soenke, D. Perret, S. Rochat, A. Barrufolo, B. Salasnich, J.-L. Beuzit, K. Dohlen, D. Mouillet, P. Puget, F. Wildi, M. Kasper, J.-M. Conan, C. Kulcsár, and H.-F. Raynaud, "SPHERE eXtreme AO control scheme: final performance assessment and on-sky validation of the first auto-tuned LQG based operational system," Proc. SPIE **9148**, 91480O (2014).
18. L. A. Poyneer, D. W. Palmer, B. Macintosh, D. Savransky, N. Sadakuni, S. Thomas, J.-P. Véran, K. B. Follette, A. Z. Greenbaum, S. M. Ammons, V. P. Bailey, B. Bauman, A. Cardwell, D. Dillon, D. Gavel, M. Hartung, P. Hibon, M. D. Perrin, F. T. Rantakyrö, A. Sivaramakrishnan, and J. J. Wang, "Performance of the Gemini

planet imager's adaptive optics system," Appl. Opt. **55**, 323–340 (2016).

19. C. Petit, J.-M. Conan, C. Kulcsár, and H.-F. Raynaud, "Linear quadratic Gaussian control for adaptive optics and multiconjugate adaptive optics: experimental and numerical analysis," J. Opt. Soc. Am. A **26**, 1307–1325 (2009).

20. L. Poyneer, M. van Dam, and J.-P. Véran, "Experimental verification of the frozen flow atmospheric turbulence assumption with use of astronomical adaptive optics telemetry," J. Opt. Soc. Am. A **26**, 833–846 (2009).

21. N. A. Bharmal, "Frozen flow or not? Investigating the predictability of the atmosphere," J. Phys. Conf. Ser. **595**, 012003 (2015).

22. L. A. Poyneer, B. A. Macintosh, and J.-P. Véran, "Fourier transform wavefront control with adaptive prediction of the atmosphere," J. Opt. Soc. Am. A **24**, 2645–2660 (2007).

23. R. Juvénal, C. Kulcsár, H.-F. Raynaud, and J.-M. Conan, "LQG adaptive optics control with wind-dependent turbulent models," Proc. SPIE **9909**, 99090M (2016).

24. P. Piatrou and M. C. Roggemann, "Performance study of Kalman filter controller for multiconjugate adaptive optics," Appl. Opt. **46**, 1446–1455 (2007).

25. C. M. Correia, K. Jackson, J.-P. Véran, D. Andersen, O. Lardière, and C. Bradley, "Spatio-angular minimum-variance tomographic controller for multi-object adaptive-optics systems," Appl. Opt. **54**, 5281–5290 (2015).

26. L. Gilles, P. Massioni, C. Kulcsár, H.-F. Raynaud, and B. Ellerbroek, "Distributed Kalman filtering compared to Fourier domain preconditioned conjugate gradient for laser guide star tomography on extremely large telescopes," J. Opt. Soc. Am. A **30**, 898–909 (2013).

27. P. Massioni, L. Gilles, and B. Ellerbroek, "Adaptive distributed Kalman filtering with wind estimation for astronomical adaptive optics," J. Opt. Soc. Am. A **32**, 2353–2364 (2015).

28. C. Correia, K. Jackson, J.-P. Véran, D. Andersen, O. Lardière, and C. Bradley, "Static and predictive tomographic reconstruction for wide-field multi-object adaptive optics systems," J. Opt. Soc. Am. A **31**, 101–113 (2014).

29. K. Jackson, C. Correia, O. Lardière, D. Andersen, and C. Bradley, "Linear prediction of atmospheric wave-fronts for tomographic adaptive optics systems: modelling and robustness assessment," Opt. Lett. **40**, 143–146 (2015).

30. E. Gendron and P. Léna, "Single layer atmospheric turbulence demonstrated by adaptive optics observations," Astrophys. Space Sci. **239**, 221–228 (1996).

31. R. Avila, J. Vernin, and E. Masciadri, "Whole atmospheric-turbulence profiling with generalized SCIDAR," Appl. Opt. **36**, 7898–7905 (1997).

32. J. Osborn, T. Butterley, M. Townson, A. Reeves, T. Morris, and R. Wilson, "Turbulence velocity profiling for high sensitivity and vertical-resolution atmospheric characterization with Stereo-SCIDAR," Mon. Not. R. Astron. Soc. **464**, 3998–4007 (2016).

33. G. Sivo, A. Turchi, E. Masciadri, A. Guesalaga, and B. Neichel, "Towards an automatic wind speed and direction profiler for wide field adaptive optics systems," Mon. Not. R. Astron. Soc. **476**, 999–1009 (2018).

34. R. Conan and C. Correia, "Object-oriented Matlab adaptive optics toolbox," Proc. SPIE **9148**, 91486C (2014).

35. M. Copeland, F. Bennet, A. Zovaro, F. Rigaut, P. Piatrou, V. Korkiakoski, and C. Smith, "Adaptive optics for satellite and debris imaging in LEO and GEO," in *Advanced Maui Optical and Space Surveillance Technologies Conference* (2016).

36. C. Correia, H.-F. Raynaud, C. Kulcsár, and J.-M. Conan, "On the optimal reconstruction and control of adaptive optical systems with mirror dynamics," J. Opt. Soc. Am. A **27**, 333–349 (2010).

37. V. Kucera, *Analysis and Design of Discrete Linear Control Systems* (Prentice Hall, 1991).

38. D. T. Gavel and D. Wiberg, "Toward Strehl-optimizing adaptive optics controllers," Proc. SPIE **4839**, 890–902 (2003).

39. L. Poyneer and J.-P. Véran, "Predictive wavefront control for adaptive optics with arbitrary control loop delays," J. Opt. Soc. Am. A **25**, 1486–1496 (2008).

40. S. M. Ammons, L. Poyneer, D. T. Gavel, R. Kupke, C. E. Max, and L. Johnson, "Evidence that wind prediction with multiple guide stars reduces tomographic errors and expands MOAO field of regard," Proc. SPIE **8447**, 84471U (2012).

41. J. Cranney, J. De Dona, V. Korkiakoski, and F. Rigaut, "An integrated identification and predictive control strategy for high wind velocity adaptive optics applications," Proc. SPIE **10703**, 107034U (2018).

42. F. Assémat, R. Wilson, and E. Gendron, "Method for simulating infinitely long and non stationary phase screens with optimized memory storage," Opt. Express **14**, 988–999 (2006).

43. D. L. Fried and T. Clark, "Extruding Kolmogorov-type phase screen ribbons," J. Opt. Soc. Am. A **25**, 463–468 (2008).

44. P. Massioni, C. Kulcsár, H.-F. Raynaud, and J.-M. Conan, "Fast computation of an optimal controller for large-scale adaptive optics," J. Opt. Soc. Am. A **28**, 2298–2309 (2011).

45. R. Juvénal, C. Kulcsár, H.-F. Raynaud, and J.-M. Conan, "Linear controller error budget assessment for classical adaptive optics systems," J. Opt. Soc. Am. A **35**, 1465–1476 (2018).

46. C. Kulcsár, H.-F. Raynaud, J.-M. Conan, C. Correia, and C. Petit, "Control design and turbulent phase models in adaptive optics: a state-space interpretation," in *Adaptive Optics: Methods, Analysis and Applications* (Optical Society of America, 2009), paper AOWB1.

47. M. S. Fadali and A. Visioli, *Digital Control Engineering: Analysis and Design*, 2nd ed. (Academic, 2012).

48. H. Shepherd, J. Osborn, R. Wilson, T. Butterley, R. Avila, V. Dhillon, and T. Morris, "Stereo-SCIDAR: optical turbulence profiling with high sensitivity using a modified SCIDAR instrument," Mon. Not. R. Astron. Soc. **437**, 3568–3577 (2013).

49. F. Roddier, J. Gilli, and G. Lund, "On the origin of speckle boiling and its effects in stellar speckle interferometry," J. Opt. **13**, 263 (1982).

50. H. Ltaief, A. Charara, D. Gratadour, N. Doucet, B. Hadri, E. Gendron, S. Feki, and D. Keyes, "Real-time massively distributed multi-object adaptive optics simulations for the European extremely large telescope," in *IEEE International Parallel and Distributed Processing Symposium (IPDPS)* (IEEE, 2018), pp. 75–84.

51. F. Ferreiraa, A. Sevina, J. Bernarda, and D. Gratadoura, "MICADO-MAORY SCAO RTC system prototyping: assessing the real-time capability of GPU," in *Proceedings of the AO4ELT6 conference* (2019).

52. G. Sivo, C. Kulcsár, J.-M. Conan, H.-F. Raynaud, É. Gendron, A. Basden, D. Gratadour, T. Morris, C. Petit, S. Meimon, G. Rousset, V. Garrel, N. Vincent, B. van Dam, M. Marcos, C. Eduardo, S. Rodrigo, R. Mischa, M. William, M. Cristian, H. Vanessa, K. Hardie, and C. Trujillo, "On-sky validation of an optimal LQG control with vibration mitigation: from the CANARY multi-object adaptive optics demonstrator to the Gemini multi-conjugate adaptive optics facility," in *American Astronomical Society Meeting Abstracts* (2015), vol. **225**.

53. F. Bennet, I. Price, F. Rigaut, and M. Copeland, "Satellite imaging with adaptive optics on a 1 m telescope," in *Advanced Maui Optical and Space Surveillance Technologies (AMOS) Conference* (2016).